Ionic-electronic interplay in perovskites

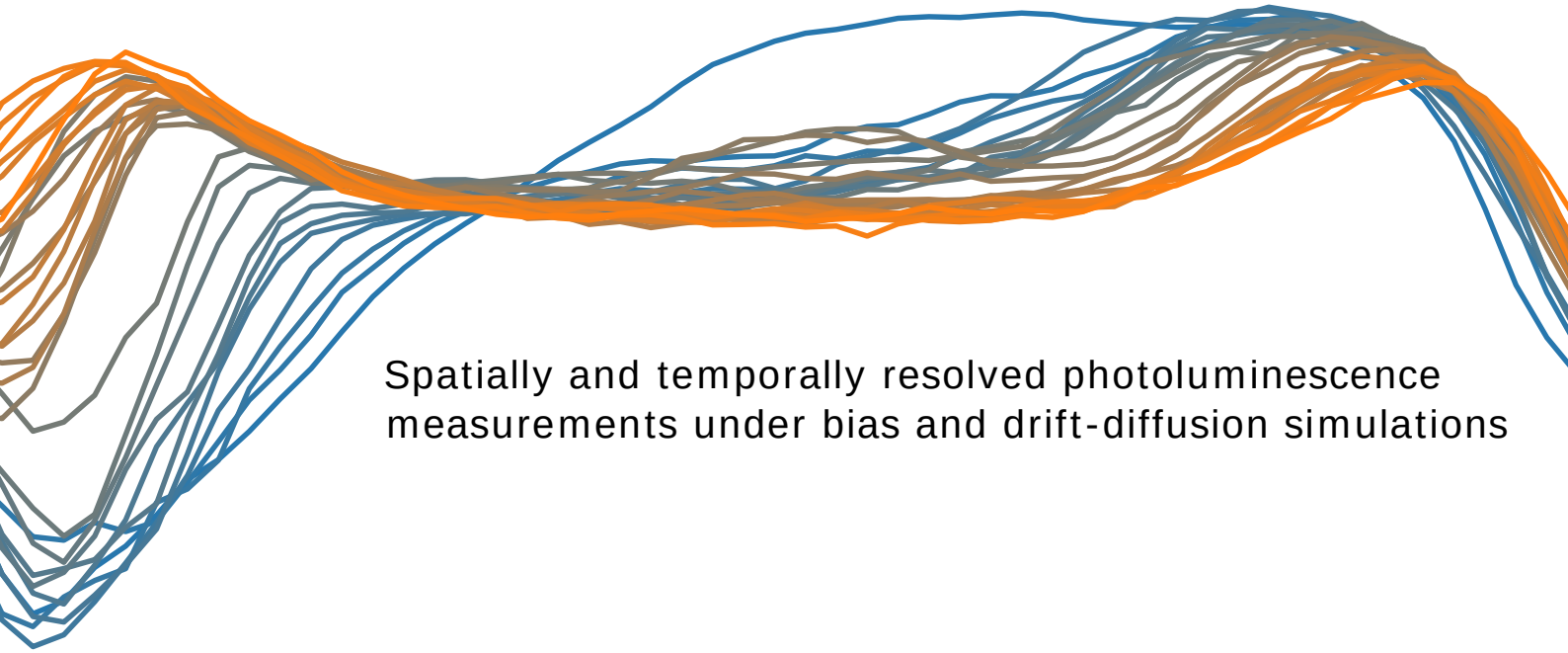

Spatially and temporally resolved photoluminescence measurements under bias and drift-diffusion simulations

Student: Federico Ravazzolo

Supervisor: Imme Schuringa

Examiners: Bruno Ehrler, Esther Alarcón Lladó

Group: Hybrid Solar Cells, AMOLF, Amsterdam

Degree: Master in Physics and Astronomy, Science for Energy and Sustainability, UvA, VU

Date of submission: 01 April 2023

Contributions and acknowledgments

The thesis is an original work, structured and written by me. However, nothing would have been possible without the Hybrid Solar Cells group. I like to think of this project as a collective effort of the whole group. A substantial part of this work emerged during intense group and subgroup meetings, colloquia, poster sessions, lunch breaks and obligatory coffee breaks. Imme Schuringa needs to be credited for conceptualizing the research question, defining the experimental methods and fabricating the device. Above all, she oversaw every aspect of the project with estimable patience and contagious curiosity. Gianluca Grimaldi made valuable contributions to the theoretical background and interpretation of the photoluminescence results. Moritz Schmidt patiently helped me with the simulations as well as having provided theoretical input and insightful feedback on the thesis and presentation. Jeroen de Boer was an essential support in the lab and gave feedback on the structure and content of the presentation. Daphne Dekker helped me maintain a high spirit inside and outside the lab. Bruno Ehrler led the entire group with a passionate, supportive and amicable attitude, always prompting in-depth discussions on the interpretation of the results

Contents

Abstract

Metal halide perovskites have been extensively investigated for their excellent photovoltaic properties. Nevertheless, ion migration decreases their long-term stability and hinders their commercialization. Understanding the interaction between ion migration and carrier distribution is crucial to identify and tackle the degradation pathways of the material. In this work, ion migration is activated by exposing an back-contact symmetric perovskite device to a bias voltage and the concentration of charges is probed indirectly through photoluminescence measurements. The photoluminescence decreases at the cathode interface and increases at the center of the device with a time scale of 40 s. This behavior is assumed to be due to the drift of a mobile anionic specie (possibly iodide) toward the cathode. Drift-diffusion simulations indicate how such an accumulation of anions could shield the field from the anode to the middle of the device and increase it at the cathode. In fact, the resulting acceleration of hole extraction at the cathode and the repulsion of electrons from the anode would explain the observed photoluminescence profile.

Introduction 1

Climate change mitigation requires the development of efficient and competitive renewable energy technologies, such as photovoltaics. Perovskites are cheap, earth abundant and efficient materials that can be used in tandem solar cells. Unfortunately, their weak ionic structure breaks down easily under exposure to environmental agents, by certain mechanisms that are not fully understood, yet.

1.1 Climate change and the energy transition

The recent IPCC report states that anthropogenic emissions of greenhouse gases have caused unprecedented climate events [1]. Surging global temperatures (fig. 1.1) lead to disastrous outcomes for earth and the ecosystems.

Rising sea levels, due to the thermal expansion of the ocean volume and the melting of glaciers are causing flooding and the destruction of the coastal habitat [3]. Moreover, the water cycle is increasing in speed and intensity, exacerbating the effects of extreme weather events. On one side, extreme precipitation like tropical cyclones, acid rains and hurricanes are intensifying [4]. Other regions are impacted by increasingly hazardous droughts, wildfires and heatwaves [5].

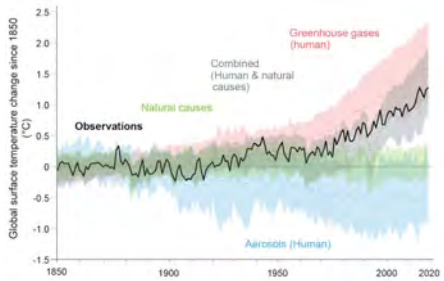

Figure 1.1: Rising global temperature and effects. [2].

Mitigating climate change, by reducing human emissions, is a priority to limit irreversible damage to human society and the natural world [6].

Where are greenhouse gas emissions coming from? The carbon footprint of an average world citizen is 13 kg of CO_2 a day. This becomes 42 kg for an American, 26 kg for a Dutch, 20 kg for a Chinese and 500 g for an Eritrean citizen [8], raising ethical concerns related to climate justice.

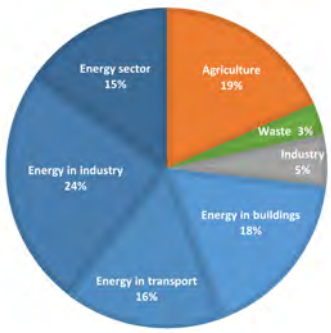

Figure 1.2: Global greenhouse gas emission by sector in 2016 adapted from [7]

Most of the greenhouse gases are generated by the energy sector. Our society is voracious for energy, mainly to manufacture infrastructures and goods, transport goods and heat households. This energy demand is still mainly sourced from fossil hydrocarbons such as coal (27 %), natural gas (23%) and oil (32 %) [9]. Fossil fuels are not only non-renewable, since there are limited reservoirs worldwide, but also non-sustainable since their combustion produces carbon dioxide as a by-product.

Affordable and reliable technologies to produce renewable energy are required to phase out fossil fuels and transition to a carbon-free economy. The major renewable energy sources are wind, solar and hydro. Hydro dominates the renewable energy share (40 %), followed by solar (28%) and wind (27 %). Nevertheless, solar energy is the fastest-growing energy technology, expanding its capacity by 19 % in 2022, followed by wind (+13 %) and hydro (+2%). [10].

1.2 Solar energy

Solar energy is a clean, renewable and abundant energy source. Every hour enough light impacts the earth's atmosphere to satisfy the energy need of humanity for a year. It can be converted into thermal energy with a solar-thermal collector [11], chemical energy with photoelectrochemical cells [12] or electrical energy with photovoltaic devices [13]. Photovoltaics are essential to support the growing electrification of the energy sector. Electricity will account for 30 % of the energy mix by 2030, according to the IEA [14].

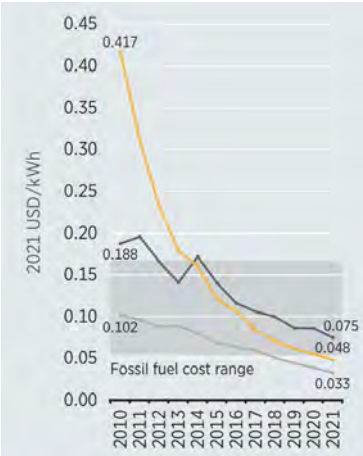

Figure 1.3: LCOE from solar (yellow), offshore wind (black) and onshore wind (gray), as reported by IRENA [15].

The crucial factors for large-scale deployment of solar cells are dispatchability, costs and environmental impacts. The seasonal and daily variability of solar irradiance limits the dispatchability of solar energy in the energy mix. Renovation of the grid infrastructure and deployment of utility-scale battery systems are required to guarantee the availability of electricity all year long.

Another leverage point to increase the capacity of solar technologies is decreasing production, installation, maintenance and disposal costs. The levelized cost of electricity (LCOE) from utility-scale solar panels dropped from 0.417 USD/kWh in 2010 to 0.048 USD/kWh in 2021, decreasing faster than any other renewable (fig. 1.3). The cost of c-Si solar cells can be reduced until a minimum threshold since the fabrication process is expensive.

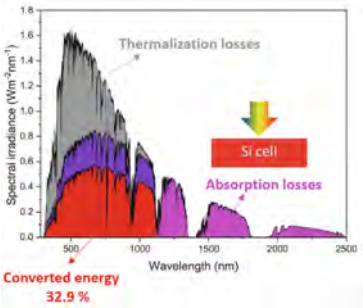

Figure 1.4: Solar spectral irradiance on the earth surface illuminating a c-Si solar cell. The ideal efficiency, 33 %, is the ratio of the extracted power (red area) by the incident power (gray area) [17].

Important factors that influence the LCOE are the lifetime and the efficiency. The longer the time of operation, the lower the LCOE since the installation investment can be repaid over a longer period. Current c-Si solar cells have a lifetime of about 25 years [16].

The efficiency of a 1.12 eV c-Si solar cells is limited to a maximum limit of 34%, because of thermalization and adsorption losses in converting photons to electrons, as shown in fig. 1.4. The performance is even lower in operating conditions, where absorption, recombination and extraction losses [18] reduce the efficiency of commercial c-Si cells to an average of 20 % [19], with a record of 27.6 % [20].

Tandem solar cells, composed of stacked junctions with different bandgaps, reach higher performances. Figure 1.5 shows how adding a 1.7 eV top layer, pushes the efficiency limit to 45 % [17]. The more layers, the higher the upper efficiency of a tandem solar cell, up to 68 % with infinite layers [21]. The highest efficiency reported in the literature to date, 47.6 %, has been reached by a 4-junction tandem cell with concentrated solar power [20].

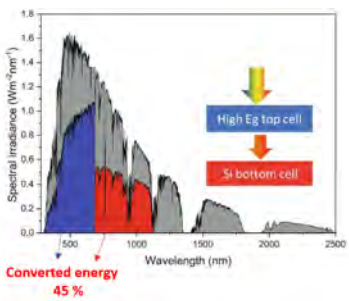

Figure 1.5: Solar spectral irradiance on the earth surface illuminating a two junction solar cell. The ideal efficiency, 45 %, is the sum of the power extracted by the top (blue area) and bottom (red area) cell divided by the incident power (gray area) [17].

Even if the environmental impact does not influence the commercialization of solar technologies it should be taken into account from an ethical point of view. Land use, landscape disruption, air pollution and the release of hazardous materials in the biosphere are the main concerns. Solar panels have a carbon footprint in the range of 14-73 g CO_2/kWh, which is still much lower than the footprint of oil (742 g CO_2/kWh) [22].

Finding efficient, stable, cheap and environmentally friendly photovoltaic materials with optimal bandgap to be inserted in tandem architectures, is a pivotal challenge for material scientists.

1.3 Perovskite solar cells

Metal halide perovskites are promising photovoltaic materials that satisfy the conditions above. Since their first appearance as a photoactive layers in 2009 [23] they have attracted increasing attention in the scientific community [24]. The efficiency of perovskite solar cells has grown from 2 % in 2012 to 25.2 % in 2021 [25], becoming the second most efficient thin film technology after GaAs [20]. All-perovskite tandems have reached an overall efficiency of 29 % [26].

Thanks to their appealing absorption, generation and extraction properties perovskites are suitable for application as wide-bandgap thin films in tandem solar cells [27]. Because of their high absorption coefficient, photons are absorbed in a few μm of material [28], allowing for ultra-thin, flexible and light films. The bandgap is direct and can vary from 1.2 eV to 3 eV [29]. By changing the chemical composition, one can tune the bandgap, and decide which wavelengths of the solar spectrum should be absorbed most efficiency. The exciton binding energy is lower than the thermal energy, 26 meV, meaning that almost every photon with energy greater than the bandgap is separated in an electron-hole pair. The generated carriers have a high mobility, long lifetime and diffusion length of up to 175 μm [30], allowing carriers to be efficiently transported to the contacts. This low recombination rate is key in defining the high efficiency of perovskites. On top of that perovskites are relatively simple and cheap to fabricate through solution chemistry at room temperature [31]. Perovskite thin films are fabricated with low quantities of the earth-abundant materials, allowing for sustainable and low-cost production.

The major drawback of perovskites that hinders their commercialization is their poor long-term stability. Perovskites are ionic materials, hence they easily degrade when exposed to humidity [32] or to the oxygen in the air [33]. Even though, encapsulation can slow down degradation up to 4 times [34], it can not slow down the degradation due to the temperature [35], electric field and light [36]. The stability has been improved over the years, reaching a record T80 (time to reduce the power conversion efficiency by 20 %) of 8000 hours [37]. Even though five devices [38][39][40][41][42] have made it past six months, perovskites are far from competing with the 20-25 years lifetime of c-Si cells. Even if degradation pathways have been attributed to the migration of ions in the perovskite, as discussed in section 1.5, there is not a comprehensive and shared understanding of the physical processes underlying their instability. The situation is aggravated by the fact that less than 20 % of the works on perovskite devices report any stability measurement [24] and only a small fraction follows the official ISOS stipulated in 2020 [43]. Another aspect that is hindering the commercialization and acceptance of perovskite solar cells is the toxicity of lead (Pb). Many attempts are being made to optimize the performance of more environmentally friendly substitutes, like Sn, Sb or Bi, not achieving competitiveness yet [44]. Also, the solvents used in the precursors' preparation raise concerns for health and the environment, even though less harmful alternatives are being investigated [45]

1.4 Materials and structure

Perovskites are a class of materials with a typical ABX_3 crystal structure (fig. 1.6). In metal halide perovskites, specifically used in solar cells, A^+ is an inorganic cation or a small organic molecule, B^{2+} is a transition metal and X^- is halogen anion [46].

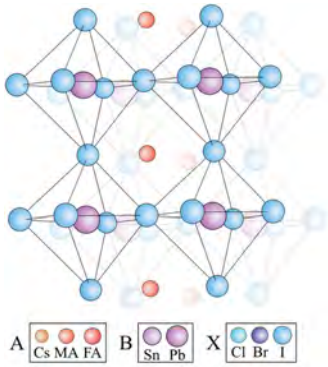

Figure 1.6: Perovskite structure and most common elements with optimal tolerance factor [47].

The bivalent cation B (mostly Pb^{2+} but more recently Sn^{2+} is also being investigated) is enclosed by a halide (Cl^-, Br^- or I^-) octahedron X_6^-. The A cation is locked in the network of octahedra by the hydrogen bond with the halides. Thus it can have a maximum radius of 2.6Å, restricting the range of possible elements to small inorganic atoms like Cesium (Cs^+) or organic molecules like Methylammonium ($MA+$) or Formamidinium (FA^+).

Changing the composition of the perovskite allows for tuning the bandgap. The band edges are determined by the anti-bonding states of the X^- and B^{2+} orbitals. Hence varying the halide composition is the easiest way to tune the bandgap. For example, Br^- is more electronegative than I^-, and thus MAPbBr has a deeper valence band edge and wider bandgap (2.3 eV [48]) than MAPbI (1.6 eV [49]). Also the A cation can induce strains in the lattice, varying the orbital overlap and thus the bandgap [50]. Nevertheless, changing a cation is roughly 7 times less effective in tuning the bandgap than changing a halide. In fact, substituting MA^+ with FA^+ decreases the bandgap by 0.1 eV [51].

The first and most widely studied perovskite is $MAPbI_3$. However, it suffers from poor stability mainly because of thermal volatilization of the organic cation and deprotonation after exposure to humidity [52]. On top of that, the bandgap is not the optimal bandgap for application for Si-perovskite tandem devices (1.7-1.8 eV [17]). The thermal and photo-instability of MA-based perovskites can be reduced by substituting the cation with FA^+ [51]. Nevertheless the FA^+ cation is affected by phase instability, especially for iodide stoichiometry between 0.3 and 0.6, because of the coexistence of a trigonal phase (typical of iodide) and cubic phase (typical of bromide) [53].

For this reason, the field is now shifting attention to more compositionally complex 'mixed-perovskites'. Mixing halides allows for tuning the bandgap to the target value for tandem devices. The first mixed-halide perovskite $MAPb(I_{1-x}Br_x)_3$ was reported in 2013 [54]. Additionally, mixing cations by incorporating cesium (Cs^+) in the recipe, improves the resistance to heat, moisture and light and electric field [55]. Hence, mixed-halide and mixed-cation perovskites, like $FA_{1-y}Cs_yPb(I_{1-x}Br_x)_3$ used in this work, have been intensively researched because of their improved stability and tunable bandgap.

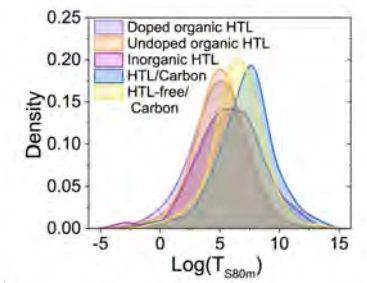

Figure 1.7: Statistical distribution of thermal stability based on the HTL type [56].

In a perovskite solar cell, the perovskite is typically sandwiched between a hole transport layer and an electron transport layer, to effectively extract charge carriers. Inorganic hole transport layers are not only cheap and easy to fabricate but also show high conductivity and relatively higher thermal stability than organic ones [56], as shown in figure 1.7. P-doped NiOx has been widely used as a hole transport layer, and will be employed in this work, because the valence band is thought to be aligned with the perovskite valence band, efficiently extracting holes.

1.5 Ion migration

Despite the progresses in increasing the stability of perovskites, the inherent instability of perovskites due to their ionic structure, is still hindering its practical implementation. The migration of ions can induce changes in the local stoichiometry, phase segregation and current-voltage hysteresis. Beside these reversible physical effects, ions can also engage in chemical reactions with the transport layers or the contacts, creating energy barriers at the interface, limiting the extraction efficiency and thus irreversibly degrading the performance of the cell [57]. Ion migration can also have beneficial effects on the performance, passivating traps and thus decreasing non-radiative recombination losses [58].

It is natural to wonder which ionic species move. The activation energy (E_A) gives information on the energy needed to mobilitate an ion. Besides Pb^{2+}, which has a high activation energy, all other cations and anions can in principle migrate, as shown in the picture on the side [57]. Iodide has low activation energy (0.58 eV [59]) and can initiate phase segregation in mixed-halide compounds, as well as react with the silver contacts creating AgI [60]. Among the cations, the migration of MA^+ (0.84 eV [59]) is imputed to trigger degradation processes [61], while adding FA^+ increases the activation barrier [62]. Other extrinsic ions can migrate too, as shown in fig. 1.8.

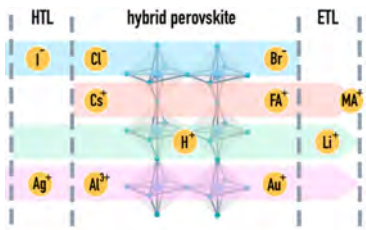

Figure 1.8: Moving ionic species and penetration in the transport layer [57].

The picture is even more complicated if one considers that beside interstitial ions (i.e. I^-), also vacancies (i.e. V_I^+) can migrate with comparable activation energies [63] [64]. In fact, moving ions and vacancies can originate from Schottky or Frenkel defects. A Frenkel defect is neutral and can form when an ion sitting in the crystal lattice is displaced, forming an interstitial defect and a vacancy. A Schottky defect is not neutral and it is formed in the crystallization process, such as a dangling bond in the crystal lattice that constitutes a vacancy.

1.6 Phlotoluminescence under bias

Characterizing ion migration in perovskites has been object of intense efforts of researchers, that used a great variety of experimental approaches: Auger Electron Spectroscopy [65], Energy Dispersive X-ray [66], Kelvin Probe Force Microscopy [67], Impedance Spectroscopy [68], Secondary Ion Mass Spectroscopy [69] and Atomic Force Microscopy [70] among the others. Another common technique to probe ion migration is the study of photoluminescence transients under bias [71] [72] [61] [73].

Photoluminescence measurements consist of shining light with a focused laser on a material and counting the emitted photons with a spectrometer. Incident photons with energy bigger than the bandgap energy create an electron-hole pair. If the electron and hole recombine radiatively they emit a photon with energy equal to the bandgap energy. The intensity of the photoluminescence signal gives information on the concentration of carriers along the device, since photons are emitted at a rate.

$$R_d = k_2 np = k_2 n_0 p_0 e^{\Delta E_F/kT}$$

Moreover, the PL gives information on the performance of the cell, since the quasi-Fermi level splitting determines the open circuit potential and thus the efficiency.

Two competitive mechanisms contribute to the reduction of photoluminescence: non radiative recombination and charge extraction. At open circuit, the photoluminescence quenching is not desired, since it is due to high non-radiative trap-assisted recombination. On the other hand, under operating conditions, a photoluminescence quenching is desired, since it means that charges are extracted efficiently [74].

Photoluminescence measurements under bias have been widely employed to observe the movement of ions indirectly, from the way ions modify the distribution of charges in the device, and hence the PL. A brief review of the main works on photoluminescence under bias will follow. The goal is to show 1) how contraddictory results and interpretations have been proposed in the past and 2) what are the open questions that this thesis is addressing.

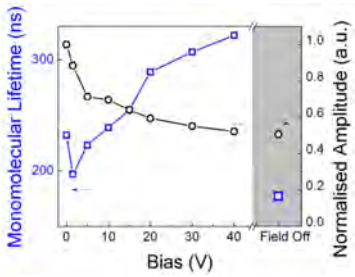

Figure 1.9: PL amplitude and extracted lifetime of carriers in a MAPI device under exposure to a bias at RT [75]

Leitens et. al in 2015 [75] showed that, at room temperature, both the radiative recombination rate and hence the photoluminescence are reduced under exposure to the electric field (fig. 1.9). Additionally, the PL is quenched for tens of seconds after the voltage is brought back to zero. They attributed this behaviour to the migration of charged defects, which increases the trap density and the monomolecular recombination rate, quenching the PL intensity and shortening the lifetime [76].

Also Deng et al. in 2016 attributed the reversible PL quenching under bias in MAPI to the migration and accumulation of ions [77]. In the same year, Jacobs et. al observed long lasting (100 s) quenching of the PL under bias. They ascribed the reversible PL responses to traps while the irreversible response to the migration of ions [78].

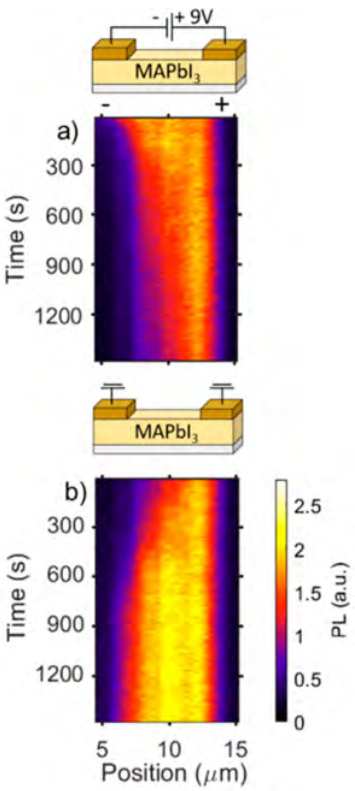

Figure 1.10: PL transient of a 15 μm MAPI lateral device, under 9V bias (adapted from [75]).

Senocrate et al. in 2017, claimed that iodide anions are the main mobile specie in MAPI and that mobility is enhanced by illumination. The material polarized under the application of an external field (hence during operation), due to the migration of of charged interstitial iodide [79]. In the same year, also Li et al. attributed the observed movement of a "dark area" on MAPI under electric field of to the migration of iodides [80]. One year after, the same group measured the time evolution of the photoluminescence under bias, along different perovskite films, attributing it to the migration of positive halide vacancies. Their proposed mechanism predicts that vacancies create local traps, increasing non-radiative recombination and thus reversibly quenching the PL. For a mixed-halide and mixed-cation perovskite $FA_{0.95}Cs_{0.05}PbI_{2.7}Br_{0.3}$, similar to the composition used in this work, the dark front moved at $3\mu s^{-1}$ after poling the film with an average electric field of $10^5 V/m$ [81].

In 2018, Birkhold et. al, have shown that the creation of interface traps depends on the injection of carriers from the transport layer, suggesting that the reduction of lead P^{2+} in P_0 and thus the removal of a lead atom from the lattice, forming a Frenkel defect, is the major defect-formation mechannism in MAPI. In the same article a spatial map of the PL under bias is reported (fig. 1.10), where a dark region expands from the negative side to the middle of the device [82].

1.7 Drift-diffusion models

Drift-diffusion models of perovskite devices have been widely employed to simulate the J-V characteristic as well as other experimental results. [83] [84] [85]. These models couple the ionic-carrier conductivity of pervoskite materials. Typically one ionic specie is assumed to be mobile and another immobile [63], while in some cases ionic species with opposite signs are given non zero mobility [86]. The model used in this work is ZimT, developed by Koopman et al. [87] and previously used to study the effect on the efficiency of recombination [88] [89], its competition with extraction [90], mobility [91], density of states [92] and transport layers [93].

Theoretical background 2

This section is meant to lay some theoretical foundations on the physics of carrier generation, recombination and transport, as well as a simple analytical description of ion migration and field screening. It is not necessary to follow the rest of the thesis, but will help grasping the results and interpretations presented later.

2.1 Energy diagram and charge concentrations

In an isolated atom or molecule, the electron can access a limited number of energy states. The periodic structure of the material introduced a continuous range of allowed energy states (energy bands) and a range of forbidden energy states (band gap). Valence electrons are bonded to the lattice and have a maximum energy E_V. Free electrons in the conduction band have a minimum energy E_B. The energy difference between the band edges is called band gap energy E_G.

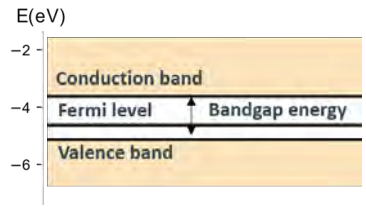

Figure 2.1: Energy diagram of a perovskite layer in the dark and at open circuit.

Given the average electrochemical potential of the electrons in the material, Fermi energy E_F, the concentration of electrons and holes are given respectively by

$$n_0 = N_C e^{-\beta(E_C - E_F)} \qquad p_0 = N_V e^{-\beta(E_F - E_V)} \tag{2.1}$$

where $\beta = 1/kT$ and N_C and N_V are the effective densities of states, computed as

$$N_C = 2\left(\frac{2\pi m_n^*}{\beta h^2}\right)^{3/2} \qquad N_V = 2\left(\frac{2\pi m_p^*}{\beta h^2}\right)^{3/2} \tag{2.2}$$

The effective masses reported in literature vary widely for different perovskites, between 0.169 and 1.5 for electrons and between 0.07 and 0.17 for holes for different. Assuming the the following effective masses $m_n^* = 1$ and $m_h^* = 0.1$, the densities of state become $N_C = 3 \cdot 10^{19}\ \mathrm{cm}^{-3}$ and $N_V = 1.5 \cdot 10^{19}\ \mathrm{cm}^{-3}$.

In a p doped material, negatively charged acceptors, capture electrons, leaving a hole in the valence band. The concentration of holes p increases, decreasing the numerator in 2.1 and thus the Fermi level gets closer to the conduction band.
At thermal equilibrium, with no illumination, the product of electron and hole density is a constant

$$n_0 p_0 = N_C N_V e^{-\beta E_G} \tag{2.3}$$

2.2 Carrier generation

When a semiconductor is shined by light, every photon with energy $h\nu > E_G$ generates an electron-hole pair. The excess energy is lost by the photogenerated charge carriers by collision with the lattice. Electrons and hole concentrations are described by two different quasi-Fermi levels

$$n = N_C e^{-\beta(E_C - E_{Fn})} \qquad p = N_V e^{-\beta(E_{Fp} - E_V)} \tag{2.4}$$

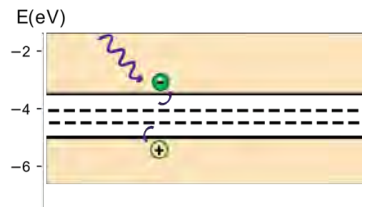

Figure 2.2: Energy diagram of a perovskite layer under illumination. An incident photon with energy bigger than the bandgap generates an electron in the conduction band and a hole in the valence band.

Under non-equilibrium, the product of the two gives

$$np = n_0 p_0 e^{-\beta \Delta E_F} \tag{2.5}$$

where the quasi fermi-level splitting is the electrochemical energy generated by the light source and can be expressed as the open circuit voltage $\Delta E_F = E_{Fp} - E_{Fn} = eV_{OC}$. The open circuit voltage is a key element in the efficiency of a photovoltaic device

$$\eta = FF \frac{V_{OC} J_{SC}}{I_{in}} \tag{2.6}$$

2.3 Carrier transport

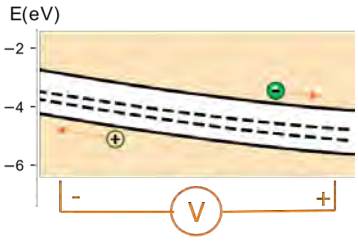

Figure 2.3: Energy diagram of a perovskite layer under illumination and bias. Generated electrons (holes) drift towards the anode (cathode).

The movement of carriers in a semiconductor can be modelled as the superposition of a electrodynamic movement, drift, and a thermal movement, diffusion. Drift is the motion of charged particles under an electric field. Negatively charged electrons move against the electric field or in the direction of the potential gradient (against an energy gradient, thus down an energy slope) with a velocity $v = -\mu_n E = \mu_n \nabla V$. The electron flux is then

$$\varphi_{n,drift} = nv = n\mu_n \nabla V \tag{2.7}$$

where the mobility depends on both the temperature and doping density that can increase the rate of collisions with the crystal lattice

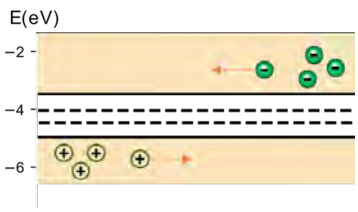

Figure 2.4: Electrons (holes) accumulated at the anode (cathode) diffuse away from the high concentration region until they are evenly distributed across the device.

Random thermal motion tends to spread out particles, thus creating a flow of electrons against their concentration gradient.

$$\varphi_{n,diff} = -D_n \nabla n = -\frac{kT}{e} \mu_n \nabla n \tag{2.8}$$

where the diffusion coefficient has been expressed in terms of mobility using Einstein relationship

$$\frac{D}{\mu} = \frac{kT}{e} \tag{2.9}$$

The electron contribution to the current density is the charge multiplied by the electric drift and diffusion flux, hence

$$J_n = -e\mu_n n \nabla V + kT\mu_n \nabla n \tag{2.10}$$

Analogously the hole contribution to the current density is

$$J_p = -e\mu_p p \nabla V - kT\mu_p \nabla p \tag{2.11}$$

Assuming $\mu = 20 cm^{-2}/Vs$ and $L = 3\mu m$ [53], the diffusion coefficient through Einstein relationship (2.9) can be estimated to be $D \simeq 0.5 cm^2/s$.

2.4 Carrier recombination

Direct recombination is a bimolecular recombination process. At thermal equilibrium the generation and recombination rates are equal

$$R_{th} = G_{th} = k_2 n_0 p_0 \tag{2.12}$$

Under illumination, the generation rate G and recombination rates R will increase and be equal in the steady state.

$$R = G = k_2 np \tag{2.13}$$

The net direct band to band recombination rate is thus

$$R_2 = R - R_{th} = k_2(np - n_0 p_0) \tag{2.14}$$

In a p-type semiconductor in low-injection regime $p \simeq p_0$ thus

$$R_2 = k_2 p_0 (n - n_0) = \frac{n - n_0}{\tau_n} \tag{2.15}$$

where τ_n is the minority carrier lifetime due to direct recombination.

The minority carrier diffusion length can be estimated as

$$L_n = \sqrt{D_n \tau_n} = \sqrt{\frac{D_n}{k_2 p_0}} \tag{2.16}$$

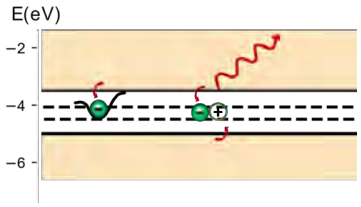

Figure 2.5: Energy diagram of a perovskite layer under illumination. An electron (hole) can recombine non-radiatively with a trap (left), or recombine radiatively with a hole, emitting a photon with energy close to the bandgap energy.

Assuming $L = 3\mu m$ [53], and $D = 0.5 cm^2 s$ as calculated before, and that the major recombination process is radiative, the minority carrier lifetime can be estimated to be $\tau_n = L^2/D_n = 18\mu s$

When an electron or a hole is captured by a trap energy state E_T (impurity o lattice defect) in the bulk it doesn't emit light. The recombination rate has a complicated dependency on the charges

$$R_{bulk} = v_{th} \sigma N_T \frac{np - n_0 p_0}{n + p + 2\sqrt{n_0 p_0} \cosh(\frac{E_T - E_F}{kT})} \tag{2.17}$$

where v_{th} is the thermal velocity, and N_T is the trap density. In a p-type semiconductor with low-injection rate the previous expression simplifies to

$$R_{bulk} = c_n N_T (n - n_0) = \frac{n - n_0}{\tau_n} \tag{2.18}$$

where τ_n is the recombination lifetime for electrons.

Dangling bonds in the interface between the perovskite and the transport layer create surface trap states where electrons and holes can recombine. In a p-type material the surface recombination rate R_{surf} is proportional to $(n - n_0)$. Hence, bulk and surface trap-assisted recombinations are both monomolecular processes. The rates can be condensed in a simple expression for a p-type material under low injection

$$R_1 = R_{bulk} + R_{surf} = k_1(n - n_0) \simeq k_1 n \tag{2.19}$$

where the approximation $n >> n_0$ works in the high injection regime. Auger recombination involves three particles. When recombining, an electron-hole pair can transfer energy and momentum to an electron (hole) in the conduction (valence) band.

2.5 Electrostatics

The electric field moves ions and charge carriers, while charge carriers deform the electric field (hence the voltage and the band structure). Generation G, recombination R and transport J vary the local charge concentration, according to the continuity equation

$$\frac{dn}{dt} = \frac{1}{e}\nabla J_n + G - R \tag{2.20}$$

An equivalent equation holds for holes as well. Poisson equation defines how a charge density ρ modifies the potential

$$\nabla \cdot \mathbf{E} = -\nabla^2 V = \frac{\rho}{\varepsilon} \tag{2.21}$$

In a region where positive charges accumulate, the electric field tends to point away from the center of the charge distribution (positive divergence). The potential will form a hill, pushing positive charges away and attracting negative charges to the center.

2.6 Electrostatics of ions

How does Poisson equation apply to a perovskite device? Let's make some assumptions to be able to gain insights from analytical solutions. First, the planar symmetry of the device allows for reducing the problem to 1 dimension. The laplacian in equation 2.21 becomes a second derivative. Second, let's neglect electronic charges by assuming that the local electronic charge concentration is $\rho = 0$. This approximation is realistic in case of high injection or low doping. Under this assumption, Poisson equation becomes Laplace equation.

$$\frac{d^2V}{dx^2} = 0 \tag{2.22}$$

The electric field can be obtained by integrating twice on dx, which gives a straight line. After setting the boundary conditions, namely placing the cathode (negative electrode) on the left and the anode (positive electrode) on the right, the potential is described by

$$V = Ex \tag{2.23}$$

where E is the module of the electric field. The potential is sketched in fig. 2.6 A. The potential energy of electrons will be

$$U = -eV = -eEx \tag{2.24}$$

where -e is the charge of one electron. this is the energy profile of the conduction and valence bands of electrons.

Now, let's consider a constant concentration C^+ of positive charges q (immobile cations). Poisson equation becomes

$$\nabla^2 V = -\frac{qC^+}{\varepsilon} \tag{2.25}$$

where the right term of the equation is constant. Integrating twice the equation gives a quadratic potential. Assuming that the electric field is zero at the anode (complete screening), the potential looks like

$$V = -\frac{qC^+}{\varepsilon}(x-l)^2 + V_b \tag{2.26}$$

where l is the device length and V_b is the external bias. The electric field is maximum at the cathode and decreases linearly across the device, as sketched in fig. 2.6 B.

In the case of different mobile ionic species, one can write Poisson equation as

$$\frac{d^2V}{dx^2} = -\frac{\rho_{ion}}{\varepsilon} \tag{2.27}$$

ρ_{ion} the ionic charge density. Assuming that different ionic species with average concentration C_i and charge q_i are in thermal equilibrium and can be described by a first order Boltzmann distribution, the ionic charge density becomes

$$\rho_{ion} = \sum C_i q_i e^{-\frac{q_i V}{kT}} \simeq \sum C_i q_i \left(1 - \frac{q_i V}{kT}\right) \tag{2.28}$$

where k is the Boltzmann constant, T the temperature. Assuming that the system is neutral, the first term of the sum in 2.28 goes to zero. Substituting in equation 2.27, one obtains Debye-Huckel equation

$$\frac{d^2V}{dx^2} = \sum C_i \frac{q_i^2 V}{kT} \tag{2.29}$$

that can be rewritten as

$$\frac{d^2V}{dx^2} = \frac{V}{L_D^2} \tag{2.30}$$

where the L_D is the Debye length, defined as

$$L = \sqrt{\frac{\varepsilon KT}{\sum C_i q_i^2}} \tag{2.31}$$

Equation 2.30 admits an exponential solution with decay length L_D. In the case of mobile anions accumulating at the anode, the potential can be written as

$$V = V_b e^{\frac{x-l}{L_D}} \tag{2.32}$$

and it is sketched in fig. 2.6 C. In this case the electric field is maximum at the anode, where the ions are accumulating, and drops to zero with an exponential decay.

What would happen if there was both an immobile cation and a mobile anion? This is the case of a Frenkel defect such as a mobile interstitial I^- that is activated and leaves an immobile vacancy V_I^+ behind. This problem can not be solved analytically. A qualitative understanding could be gained assembling the two previous examples B and C. The voltage profile would be constant (zero electric field) in the middle of the device, quadratically increasing away from the anode (linearly increasing electric field) and exponentially increasing towards the cathode (exponentially increasing electric field), as sketched in fig. 2.6 D.

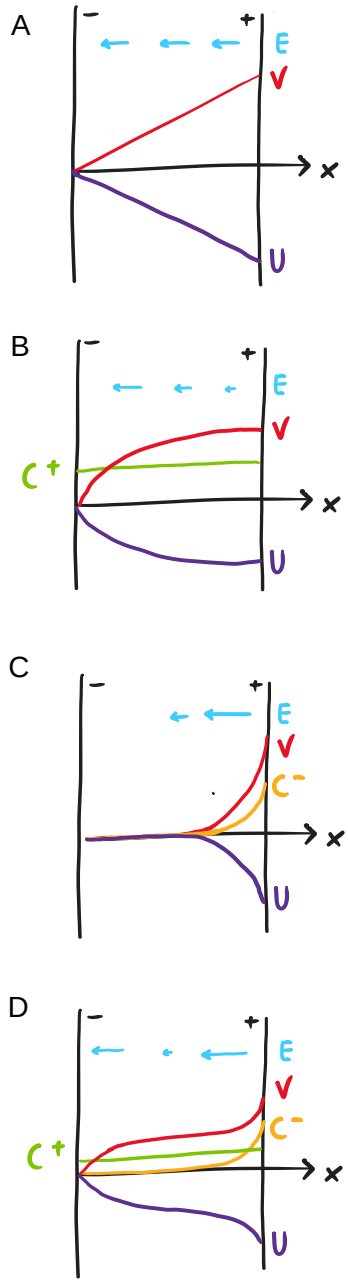

Figure 2.6: Sketch of the electric field E, electric potential V and electron potential energy U solutions of Poisson equation with an external bias. A) no ions. B) immobile cations C^+. C) mobile anions C^-. D) immobile cations and mobile anions.

Research question and methods 3

The question that this work tries to address is:

> How does ion migration influence the concentration of carriers along a perovskite device?

The first objective is to observe how carriers distribute along a perovskite layer under bias. This is done by measuring the photoluminescence transient under bias (Section 5) of a perovskite device. In this project we focus on the stable and tunable mixed-halide and mixed cation perovskite. Moreover, the fabricated device is lateral and symmetric to facilitate the optical measurements (Section 4)

The second objective is to understand how the migration and accumulation of ions, influences the distribution of carriers. This is done by performing steady-state simulations of a one dimensional symmetric perovskite device under illumination and bias. The model used includes the electrostatic effect of one free mobile anion and neglects traps and non-radiative recombination (Section 6). The research question can be rewritten in detail, incorporating the methods used in this work:

> **Can an electrostatic model explain** how ion migration influences the concentration of carriers, **by reproducing the measured photoluminescence under bias**, along a **mixed-cation mixed-halide** perovskite **symmetric lateral** device?

Device 4

In the fabricated device, a metal layer and a hole transport layer are evaporated on the substrate, previously patterned with UV-lithography. In this way the perovskite deposited on top is directly exposed to light, forming a back-contact device.

4.1 Concept

In the most simple architecture, the perovskite material is sandwiched between two selective transport layers, a hole transport layer and an electron transport layer, allowing for selective charge extraction.

In back contacts devices, instead, the conductive layers are deposited on the rear of the device, leaving the photovoltaic material directly exposed to light. Open architectures have been used recently to investigate directly the perovskite layer by probing it with photoluminescence, XRD or XRF measurements [94], [95]. On top of that they have reached great performances in c-Si devices [96], since the shading losses due to electrodes can be avoided. Additionally, there is more freedom in choosing conductive contacts with no transparency requirement.

The device that is analyzed in this work is a *symmetric interdigitated back contact device*. It is symmetric since only a hole transport layer is used. Back contact since the contacts and transport layers are deposited on the rear of the device and not on top. Interdigitated since the contact are patterned as parallel stripes or fingers (*digitus* in Latin). The cell lateral section is sketched in fig. 4.2, while a top view scheme is displayed in fig. 4.1.

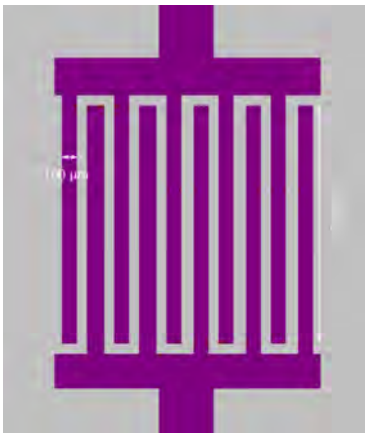

Figure 4.1: Device top-view

After imprinting the pattern on the quartz substrate using negative-resist UV lithography, the silver (Ag) contact is evaporated on top. The hole transport layer is created by first evaporating nickel (Ni) and then annealing in air to form nickel oxide (NiOx). On top of that, a layer of mixed halide and mixed cation lead perovskite ($FA_{0.83}Cs_{0.17}Pb(I_{0.6}Br_{0.4})_3$) is spin coated and then coated with a protective layer (PMMA).

Figure 4.2: Sketch of device lateral section. The sketch is not in scale. The Si layer is expected to be 100 nm thick, the NiO layer is roughly 10 nm thick.

4.2 Fabrication

First the quartz substrate is cleaned. More in detail, a 15x15 mm quartz sample is brushed with soap, sonicated in water for 10 minutes and in acetone for 8 minutes. The cleaned sample is transferred to a clean room, where it is immersed in a boiling solution with 10 ml of Ammonium hydroxide (30 %), 10 ml of Hydrogen peroxide (30 %) and 50 ml of demineralized water. This process should remove inorganic and organic residues. The cleaning procedure ends with 2 minutes of Plasma-Cleaning, to further remove organic impurities.

In the UV lithography process, a photoresist MAN1420 is spincoated over an adhesion layer HMDS and then patterned with UV light through a mask. After evaporating Ag and Ni, all the parts that didn't react with the development solution (hence the ones exposed to light), are lifted off. In detail, after HMDS is spincoated at 400 rpm for 35 s and annealed at 150 C for 1 minute, 200 µL of MAN1420 are spincoated at 3000 rpm for 30 s and annealed at 100 C for 2 minutes. The sample is covered by the mask in fig. 4.1 and exposed to 550 mJ/cm^2 of 365 nm UV light. The sample is developed for 80 s at 21 C and rinsed with demineralized water. A nanolayer of silver and nickel is precipitated on the photoresist with a rate of 0.05 1nm/s through Electron Beam Physical Vapor Deposition (EBPVD). An electron beam heats the material in a vacuum chamber, evaporating the atoms. After leaving the sample in acetone for 1 hour, and rinsing it, the non-exposed parts can be lifted off. The patterned sample is dried with a N_2 gun.

To oxidize the Ni layer, the sample is annealed in air for 20 minutes at 450 C (with additional 20 minutes of ramping up and 60 minutes of cooling down). The samples are transferred to a Nitrogen glovebox, where 65 µL of perovskite precursors solution, filtered by a 0.2 µm filter, is spincoated at 2000 rpm for 10 s and at 5000 rpm for 30 s. After 15 s from the beginning of the spincoating, the sample is quenched with an N_2 gun for 15 s at a vertical distance of 5-10 cm. After annealing the sample at 100 C for 10 minutes, 200 µL of PMMA A8 solution is spincoated at 3000 rpm for 45s and then annealed at 95 C for 5 minutes.

Table 4.1: Perovskite solution recipe and measured amount on 30/09/2022. Measured amounts are determined by reading the maximum and minimum values displayed in the balance screen up to the resolution of 0.0001 g. The relative deviation of the solvent mixture is trivially estimated from the pipette resolution 0.01 mL. The relative deviation of the solvent volumetric ratio is calculated as the ratio of pipette resolution 0.01 mL and the total volume prepared, 5 mL, hence 0.2 %.

Precursor	Nominal quantity	Measured quantity	Error
PbI_2	0.664 g	0.6648-0.6636 g	0.1 %
FAI	0.189 g	0.1894-0.1886 g	0.2 %
CsBR	0.0515 g	0.0517-0.0512 g	0.6 %
Solvent	**Nominal quantity**	**Measured quantity**	**Error**
DMF	4.5 ml	4.49-4.51 ml	-
NMP	0.5 ml	0.49-0.51 ml	
DMF and NMP	1.4 ml	1.39-1.41 ml	0.7 %
DMF and NMP	(1:9)	0.998:9.002)-(1.002:8.998)	0.2 %

Photoluminescence under bias 5

The biased perovskite device is illuminated with a laser from one contact to the other. Measuring the photoluminescence, gives information on the concentration of electrons and holes along the device. When the bias is switched on, the cathode darkens (less carriers) while the middle of the device brightens (more carriers).

5.1 Concept

The device is hit by a high energy laser that generates electron-hole pairs. The carriers recombine radiatively and the emitted photons are collected and counted by a detector for different points of the material. The counted photons are arranged in a histogram on the wavelength that assumes a gaussian shape, called photoluminescence (PL) spectrum. The peak wavelength is related to the bandgap of the material and the width of the gaussian gives information on the quality of the material. An infinite crystal would ideally emit a delta-like signal peaked at the bandgap wavelength. However, the perovskite crystalizes in grains of limited size and the signal broadens. The integral of the spectrum is the total steady-state PL and its distribution along the device gives information about the distribution of carriers since PL $\propto$ np.

The PL intensity is scanned along a line from one contact to the other, as displayed in fig. 5.1. After a line scan is finished, another scan begins, capturing the behaviour of the material at different instants (temporally resolved PL). The time-scale of a line is in the order of 6 seconds, to capture the slow dynamic of the system most likely imputable to ion migration. The charge carriers are assumed to reach equilibrium in the transition between one point and the other, since they are extracted in a much shorter timescale ($\mathrm{ns} - \mathrm{ms}$) than the sampling time 0.06s. After the first line scan, the device is poled with an external 10 V bias, to induce the drift of mobile ions. The same is repeated switching off the potential after the first scan. More details on the parameters employed during the measurements are reported in the next section.

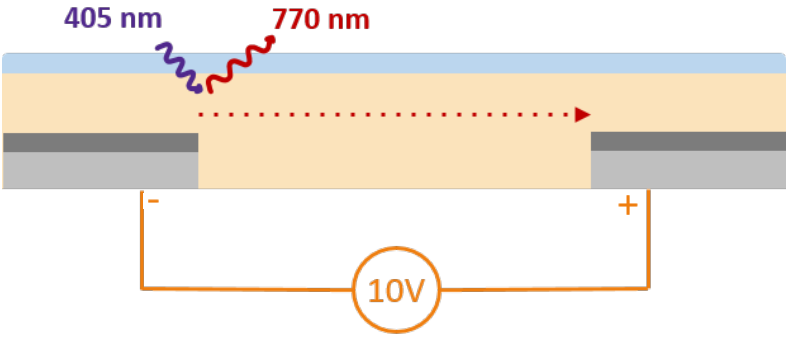

Figure 5.1: Scheme of the PL measurement under bias. The material is excited by a $405\mathrm{nm}$ laser and the emitted photons, with a wavelength distribution centered around the bandgap wavelength $770\mathrm{nm}$ are counted by the camera. The laser moves from left to right, with a speed of 1 point/0.06 s or 1 line/6 s, from the cathode to the andoe. The applied bias is $10\mathrm{V}$, forming an average electric field of $10^5\mathrm{V/m}$.

5.2 Experimental setup

The steady state PL is measured with a WITec alpha300 RS confocal microscope in reflection mode. The setup is composed of an optical microscope with a 20x objective, a coherent laser with an excitation wavelength $405\mathrm{nm}$, and a charge-coupled device (CCD) used as a detector, that captures the entire spectrum.

In one horizontal scan, the PL spectrum is measured for n_x points, at a distance dx apart from left to right. One line is then $L_x = n_x \cdot dx$ long. The stage is moved down by a distance dy for each of the n_y lines. The photons are gathered and counted for a time dt and it takes a time $d\tau$ to move the stage to the next point. Hence, the total duration of a line scan can then be estimated as

$$T = n_x(dt + d\tau) \tag{5.1}$$

and measured manually with a chronometer for small values of dt, giving $T = 6\mathrm{s}$ and thus $d\tau = 0.06\mathrm{s}$. The time dt can be adjusted to capture different timescales. In this work $dt = 0.01 - 0.02$, hence $T = 6\mathrm{s}$, is used to capture faster ion dynamics (high voltages) while $dt = 0.1\mathrm{s}$, hence $T = 16\mathrm{s}$, could be used to for lower voltages.

The formula used in the calculations on the side are

$$G = \frac{\varphi}{d} = \frac{I}{d}\frac{\lambda}{hc} \tag{5.2}$$

where $G[\mathrm{cm}^{-3}\mathrm{s}^{-1}]$ is the rate at which electrons and holes are generated, from a photon flux $\varphi[\mathrm{cm}^{-2}\mathrm{s}^{-1}]$ penetrating at a depth $d[\mathrm{cm}]$. The flux is calculated from the irradiance $I[\mathrm{Wcm}^{-2}]$ of photons with wavelenght $\lambda[\mathrm{nm}]$.

The measured laser power ($0.3\mu\mathrm{W}$ for nominal power of $0.26/\mathrm{mW}$) divided by the illuminated area, a circle of diameter $15\mu\mathrm{m}$, gives the irradiance $0.1\mathrm{Wcm}^{-2}$. Given the energy of a 405 nm photon, which is $3\mathrm{eV} = 3 \cdot 1.6 \cdot 10^{-19}\mathrm{J}$ one could calculate the photon flux which is $\varphi = 3 \cdot 10^{17}\mathrm{cm}^{-2}\mathrm{s}^{-1}$. This photon flux is comparable to the flux of adsorbed photons by a 1.6 eV perovskite under standard conditions, AM1.5, which is roughly $10^{16}\mathrm{cm}^{-2}\mathrm{s}^{-1}$. Since the measured adsorption coefficient of the perovskite is $0.3 \cdot 10^5\mathrm{cm}{-1}$, the penetration depth of light can be approximated to be $3 \cdot 10^{-5}\mathrm{cm}$. Form this one could estimate the rate at which electron-hole pairs are generated $G = 10^{22}\mathrm{cm}^{-3}\mathrm{s}^{-1}$, which is an important input of the simulations. The parameters used in the measurements are summarized in table 4.1.

A Keithley 2400 SMU, remotely controlled, is used to apply the external 10 V bias to the sample and to record the current. Before starting the measurements the quality of the contact between the probes and the cell's electrodes is checked by measuring an IV curve.

Table 5.1: Parameters used in the photoluminescence maps.

Quantity	description	Values
dx	distance bewteen points	1.75 $\mu\mathrm{m}$
dy	distance bewteen lines	5 $\mu\mathrm{m}$
nx	number of points	100
ny	number of lines	10-40
P	nominal laser power	0.2-0.5 mW
I	irradiance	0.16 Wcm^{-2}
dt	integration time	0.01 s-0.1s
V	Voltage	10 V

5.3 Data analysis

The output of the measurements is a matrix containing the photon counts PL_{ijk} where $i \in [0,n_x)$ is the index of the points, $j \in [0,n_y)$ is the index of the lines and $k \in [0,n_w)$ is the index of the wavelength.
In the continuum, the matrix becomes the function PL(x,t,λ) where the horizontal position is $x = i \cdot L_x/n_x$, the time dependency is determined as $t = j \cdot T = j \cdot n_x(dt + d\tau)$ and λ is the wavelength. The wavelength dependent spectrum can then be fitted to a gaussian curve

$$f(\lambda) = B + A\exp\left(-\left(\frac{\lambda - \lambda}{\sigma}\right)^2\right) \tag{5.3}$$

to remove the background B. A plot of the noise free and fitted spectrum, is shown in figure 5.2 for t = 0 and $x = 80\mu m$ (off contact) and $x = 150\mu m$ (over contact).

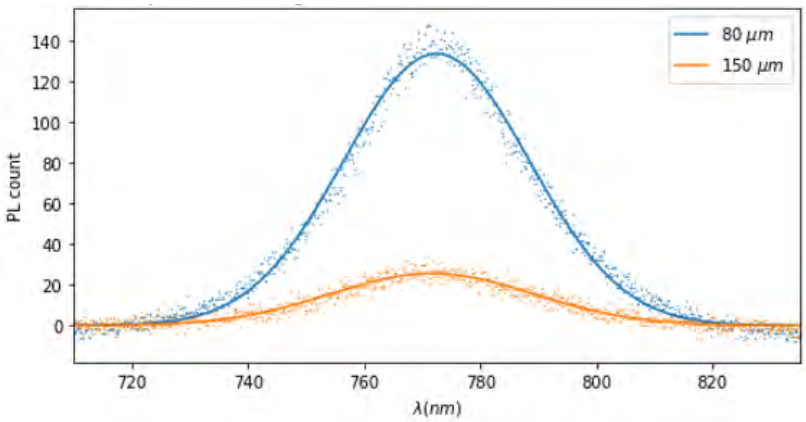

Figure 5.2: Background removed PL spectrum and fit at 0V, above the contacts (150 μm) and off the contacts (80μm).

The PL in the position x and at time t is obtained integrating, or summing, the spectrum

$$PL(x,t) = \sum_{\lambda \in \Lambda} PL(x,t,\lambda) \tag{5.4}$$

As a standard data analysis procedure the integral of the noise-free signal is plotted in the wavelength range $\Lambda = \lambda_0 \pm 50\mu m$, where λ is the central wavelenght, obtained from the fit. Moreover, all the line scans are displayed just in the perovskite $x \in [0, 100]\mu m$ and not over the contacts, since the PL over the contacts is constant and doesn't give relevant information on the interplay between ions and carriers. The measured photoluminescence doesn't depend on the scan speed or on the direction of the scan. The photoluminescence at 0V is also reproduced for three different batches, as show in section A.2. One could also plot the central wavelenght of the gaussian and would obtain a function $\lambda_0(x,t)$, that is shown in appendix A.5.

5.4 Result

The colormap PL(x,t) is displayed in fig. 5.3. On the left, the 10 V bias is applied after the first line scan from the cathode to the anode ($x = 100\mu m$) is complete (A). A bright region appears in the proximity of the anode and slowly expands to the middle of the device, while the cathode region darkens (B). After 40s the PL reaches the bias steady state (C).

On the right, the 10 V bias is switched off after the first line scan is complete (A). Now, the bright region in the middle of the device disappears, as well as the dark region close to the cathode. In the final unbiased steady state the PL is almost homogeneous, but for two brighter peaks 15 μm away from the electrodes (B). Interestingly, it takes 80 s, twice as long, for this transition to be complete (C).

Interpreting these results is not trivial and requires a deeper understanding of the system behaviour. At least, it needs to be clarified how the ion migration, activated by the external bias, influences the charge carriers distributions, and thus the photoluminescence. This will be discussed in the next session.

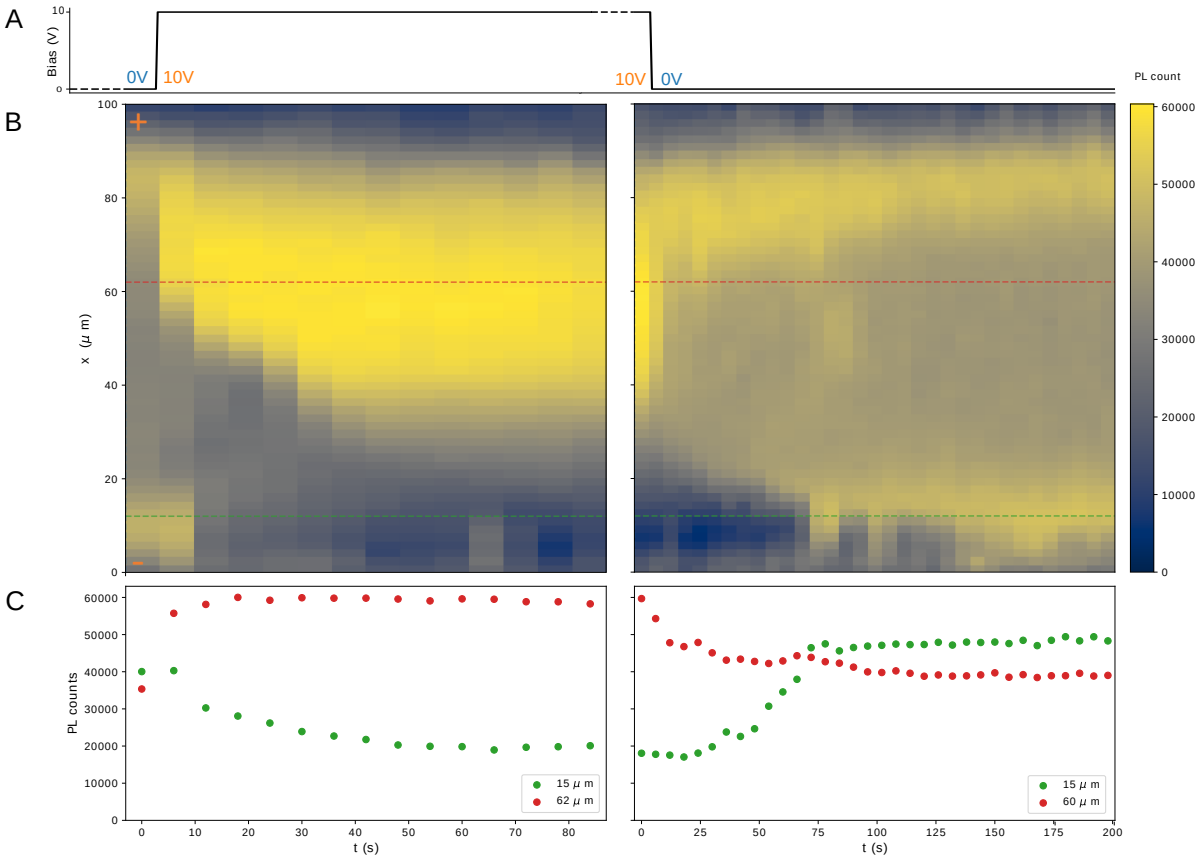

Figure 5.3: Spatially and time-resolved PL intensity under bias. **A)** The potential is switched to 10V after measuring the first column on the left graph and switched off to 0V after measuring the first column, on the right graph. **B)** The measured PL over time is mapped as a function of the position x along the device. The anode is on the top edge (x = 100 μm). The PL count is the integrated spectral photon count, after background removal. **C)** Time dependency of the PL at two fixed positions: above the 0V maximum, x = 15μm, and above the 10 V maximum = 62μm. Choosing different positions doesn't change the timescale, as shown in appendix A.3.

Simulations 6

A simple model of the device consists of mobile electrons and holes that are generated by illumination, drift under an electric field and recombine, emitting photoluminescence. At the same time, mobile negative ions can drift under the electric field and modify the electric field itself, thus changing the concentration of electrons and holes.

6.1 Concept

One dimensional time-dependent drift-diffusion simulations are based on a system of differential equations that couples the charge concentrations (ions, holes, electrons) and the potential.

First, the *drift-diffusion equation* regulates the currents based on the drift along a potential slope and a diffusion against a concentration gradient. Second, *Poission equation* accounts for charges modifying the potential. Third, the *continuity equation* updates the charge concentration based on the current density as well as the generation and recombination of electrons and holes.

The algorithm requires as an input an external voltage and an illumination profile (mimicking the photoluminescence measurement under bias) as well as some parameters like dielectric constant, band energies, density of states, of the perovskite and transport layers.

The solutions of the model can be visualized as a band diagram (fig. 6.1), that changes over time. The band energy is proportional to the electric potential and the slope gives the electric field. The electron and hole concentrations are represented by the Fermi-level (in the dark) and the quasi-Fermi levels (under illumination). The closest the Fermi level to the conduction (valence), the highest the concentration of electrons (holes).

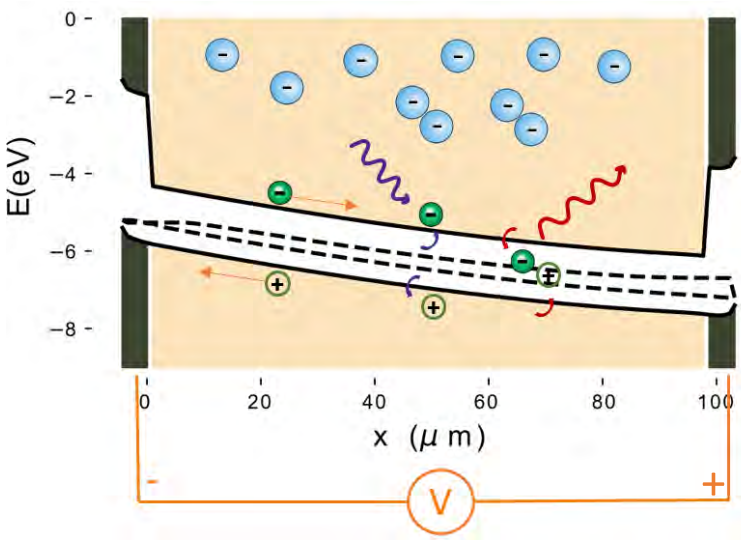

Figure 6.1: Simulated energy diagram under bias. The band diagram shows conduction band valence band and quasi-Fermi levels in the 100 μm perovskite layer (ochre) and in the 5μm hole transport layers (dark gray). The carriers (green) are generated under illumination (violet), drift under an applied bias (orange) or recombine radiatively (red).

6.2 Physical model

The simulations are performed using ZimT, an open-source code for transient drift-diffusion simulations, developed by L.J.A. Koster [97]. As mentioned in the previous section, the algorithm solves a system of coupled partial differential equations in the following variables: electron concentration $n(x,t)$, holes concentration $p(x,t)$, anions/cations concentration $C_{-/+}(x,t)$ and voltage $V(x,t)$. The first fundamental equation is the drift diffusion equation for electrons and holes (see section 2.3).

$$\begin{cases} J_n(x) = -e\mu_n \frac{\partial V(x)}{\partial x} + kT\mu_n \frac{\partial n(x)}{\partial x} \\ J_p(x) = -e\mu_p \frac{\partial V(x)}{\partial x} - kT\mu_p \frac{\partial p(x)}{\partial x} \end{cases} \tag{6.1}$$

where e is the elementary charge, $J_{n/p}(x)$ is the electron/hole current density and $\mu_{n/p}$ the electron/hole mobility, assumed to be uniform along the device. Analogously, ions' drift and diffusion motions can be described by

$$\begin{cases} J_+(x) = 0 \\ J_-(x) = -e\mu_- \frac{\partial V(x)}{\partial x} + kT\mu_- \frac{\partial C_-(x)}{\partial x} \end{cases} \tag{6.2}$$

where we have assumed one mobile anion with mobility μ_- and one immobile cation. The total current density is then given by the sum of carrier and ionic current densities

$$J(x) = J_+(x) + J_-(x) + J_n(x) + J_p(x) \tag{6.3}$$

Moreover, the concentration of electrons/holes increases if there is a current influx, increases with a rate G if photons generate carriers and decreases with a rate R if carriers recombine, as described by the continuity equations

$$\begin{cases} \frac{\partial n(x)}{\partial t} = +\frac{1}{e}\frac{\partial J_n(x)}{\partial x} + G(x) - R(x) \\ \frac{\partial p(x)}{\partial t} = -\frac{1}{e}\frac{\partial J_p(x)}{\partial x} = G(x) - R(x) \end{cases} \tag{6.4}$$

where the recombination rate is assumed to be *purely radiative*

$$R(x) = k_2(np - n_0p_0) \tag{6.5}$$

Ions can only drift and diffuse, hence, the continuity equations are trivially

$$\begin{cases} \frac{\partial C_+(x)}{\partial t} = 0 \\ \frac{\partial C_-(x)}{\partial t} = \frac{1}{e}\frac{\partial J_-(x)}{\partial x} \end{cases} \tag{6.6}$$

Finally, Poission equation assembles everything together, describing how charges modify the electric potential

$$\frac{\partial^2 V(x)}{\partial x^2} = -\frac{e}{\varepsilon}(p(x) - n(x) + C_+(x) - C_-(x)) \tag{6.7}$$

6.3 Parameters

The toy-model of our device consists of a 100 μm perovskite layer with dielectric constant $\varepsilon_r = 15$ sandwiched in between two $5\mu m$ transport layers, $\varepsilon_r = 12$. The conduction bands are aligned at $E_C = 5.4eV$ with the electrode work function, while the NiO transport layer has a wider bandgap $E_G = 3.8eV$ than the perovskite $E_G = 1.6eV$ forming an energy barrier for electrons. The perovskite is undoped while the transport layer is p-doped with acceptor concentration $N_A = 10^{12} cm^{-3}$. Charges have higher mobility in the perovskite, $\mu_{p/n} = 50 cm^2 V^{-1}$, than in the HTL, $\mu_{p/n} = 0.3 cm^2 V^{-1}$. Anions with unitary charge, move with a mobility $\mu_- = 10^{-5} cm^2 V^{-1}$ and can't penetrate the transport layer interface, while cations are immobile. The capture rate of traps is set to zero, allowing only radiative recombination. The device is biased and then illuminated with a 0.05s wide gaussian pulse. The n, p and C_- concentrations are recorded and displayed at the peak of the pulse, as in the PL measurements.

Some parameters, like anion concentration, cation concentration, illumination and voltage, are varied in the simulations to investigate the system behaviour, as discussed in Section 5.5.

Table 6.1: Simulation parameters. The columns report symbol, unity, value and source. See nomenclature section at the end of the thesis for clarification of the quantity that the symbol represents.

Perovskite			
d	μm	100	-
E_C	eV	3.8eV	[98] [99] -
E_V	eV	5.4	[100]
ε_r		15	-
$N_{C/V}$	cm^{-3}	$2 \cdot 10^{19}$	2.1
$N_{A/D}$	cm^{-3}	0	-
$\mu_{n,p}$	$cm^2 V^{-1} s^{-1}$	50	[101] [53]
$C_{+/-}$	cm^{-3}	$10^{10} - 10^{13}$	[91] [102]
μ_-	$cm^2 V^{-1} s^{-1}$	10^{-7}	-
k_2	$cm^3 s^{-1}$	10^{-14}	-
Transport layer			
d	μm	5	
E_C	eV	1.6	[103]
E_V	eV	5.4	[103]
ε_r		12	[104]
$N_{C/V}$	cm^{-3}	10^{21}	2.1
N_A	cm^{-3}	10^{12}	[105]
$\mu_{n,p}$	$cm^2 V^{-1} s^{-1}$	0.3	[106]
External parameters			
V	V	$0 - 10$	-
δt	s	0.05	-
G_{max}	$cm^{-3} s^{-1}$	$10^{10} - 10^{15}$	-

6.4 Assumptions and limitations

Limitations of the simulation that need to be taken into account are the simplistic model employed (one mobile anion, only radiative recombination) and the unrealistic parameters used (low ion concentration and low illumination).

First, assuming that ions can't react or diffuse into the transport layer could limit the reliability of the model, since ions are known to do both [60][61]. On top of that, since the activation energy and mobility of ions in mixed halide and mixed cation perovskite is still not clearly determined [57], the assumption that only I^- moves and leaves immobile Frenkel vacancies behind, could sound slander.

Moreover, assuming purely radiative recombination and neglecting the defects-mediated recombination, by setting $k_1 = 0$, is a rough assumption. In fact, ions can activate or passivate traps in the bulk or in the interface, quenching or enhancing the PL [81]. Neglecting Auger recombination is fair for low levels of injected carriers ($n < 10^{22} m^{-3}$) [107].

Second, the simulations did not converge for higher values of illumination intensity and ion concentration. In fact, the maximum generation rate tested is $10^{15} cm^{-3} s^{-1}$ while the generation rate in the PL measurements is $10^{22} cm^{-3} s^{-1}$ as calculated in section 5.3. The maximum ion concentration tested is $10^{13} cm^{-3} s^{-1}$, which is lower than the values proposed in the literature that vary from $10^{13} cm^{-3} s^{-1}$ [102], $10^{17} cm^{-3} s^{-1}$ [108] up to $10^{19} cm^{-3} s^{-1}$ [109].

Nevertheless, the purpose of this limited qualitative model is to show how the formation of dark and bright regions in the photoluminescence could be due to electrostatic effects, without involving defect chemistry or interface effects.

6.5 Results

In this section the main results of the simulations are reported. In the first simulation, the device is illuminated at different positions with a gaussian pulse of $1\mu m$ width for $0.05s$. A 2V bias is also applied, mimicking the experimental conditions. The resulting concentration np is plotted in fig. 6.2 for different excitation positions. The np concentration (and hence the photoluminescence is peaked in the center-right of the device and quenched in the center-left. This is compatible with the observed photoluminescence profile under bias.

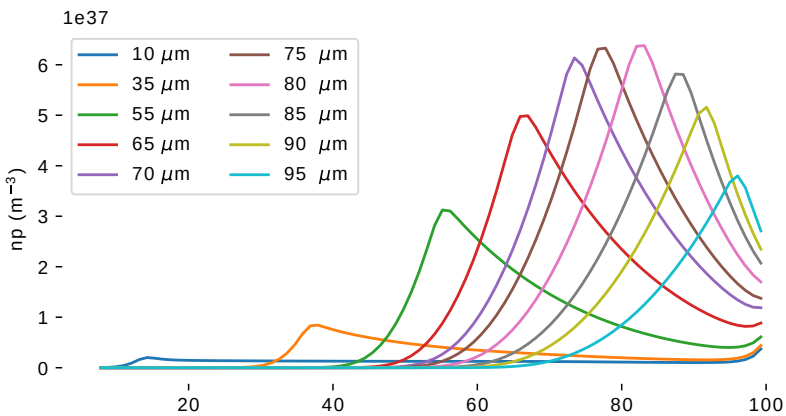

Figure 6.2: Excitation position dependent simulation. Product of electron and hole concentrations np for different excitation positions.

In all following simulations, the full device is illuminated with the same generation rate and for the same amount of time. The shape of the PL doesn't change, still peaking in center-anode and depleted at the cathode. This feature does not change when varying the voltage (fig. 6.3), illumination (fig. 6.4) or concentration of immobile cations (fig. 6.5).

Nevertheless, testing the impact of different ionic concentrations, shows how ions play a critical role in determining the peaked PL shape. As evident from figure 6.6, when the concentration of mobile anions is too low, the electrons are confined to the anode interface. Only after a certain critical concentration, electrons are repelled towards the middle of the device, forming the peaked PL profile observed in the experiments.

Some simulations at 0V were carried too, even though the algorithm diverged in many cases and for the majority of parameters tried. One result is shown in fig. 6.7 and will be further discussed in the following chapter.

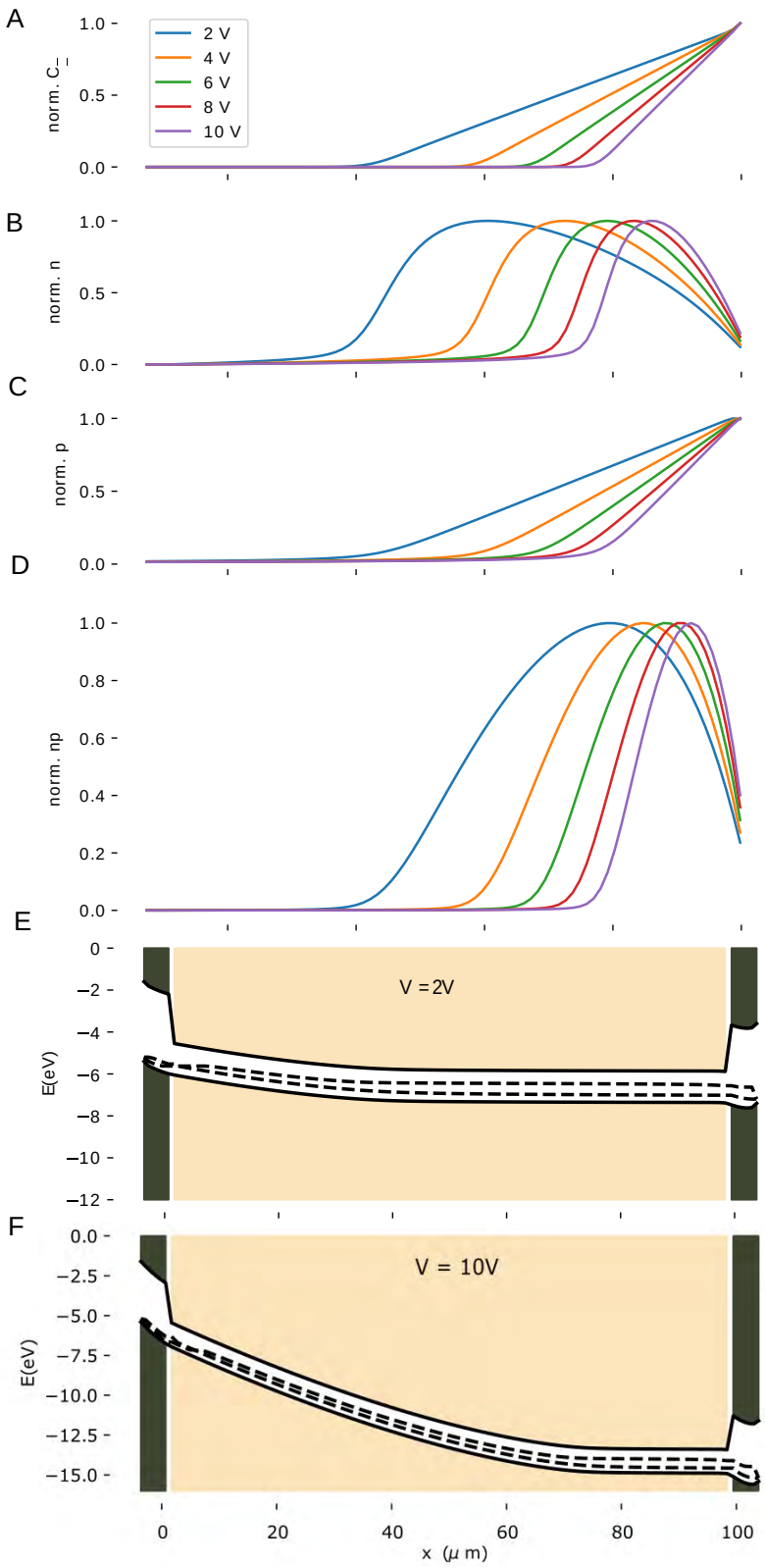

Figure 6.3: Bias dependent simulations. Normalized concentrations of mobile anions **(A)**, electrons n **(B)**, holes p **(C)** and photoluminescence np **(D)** for different external biases. Band diagrams and quasi-Fermi levels for V = 2V **(E)** and V = 10 V **(F)**.

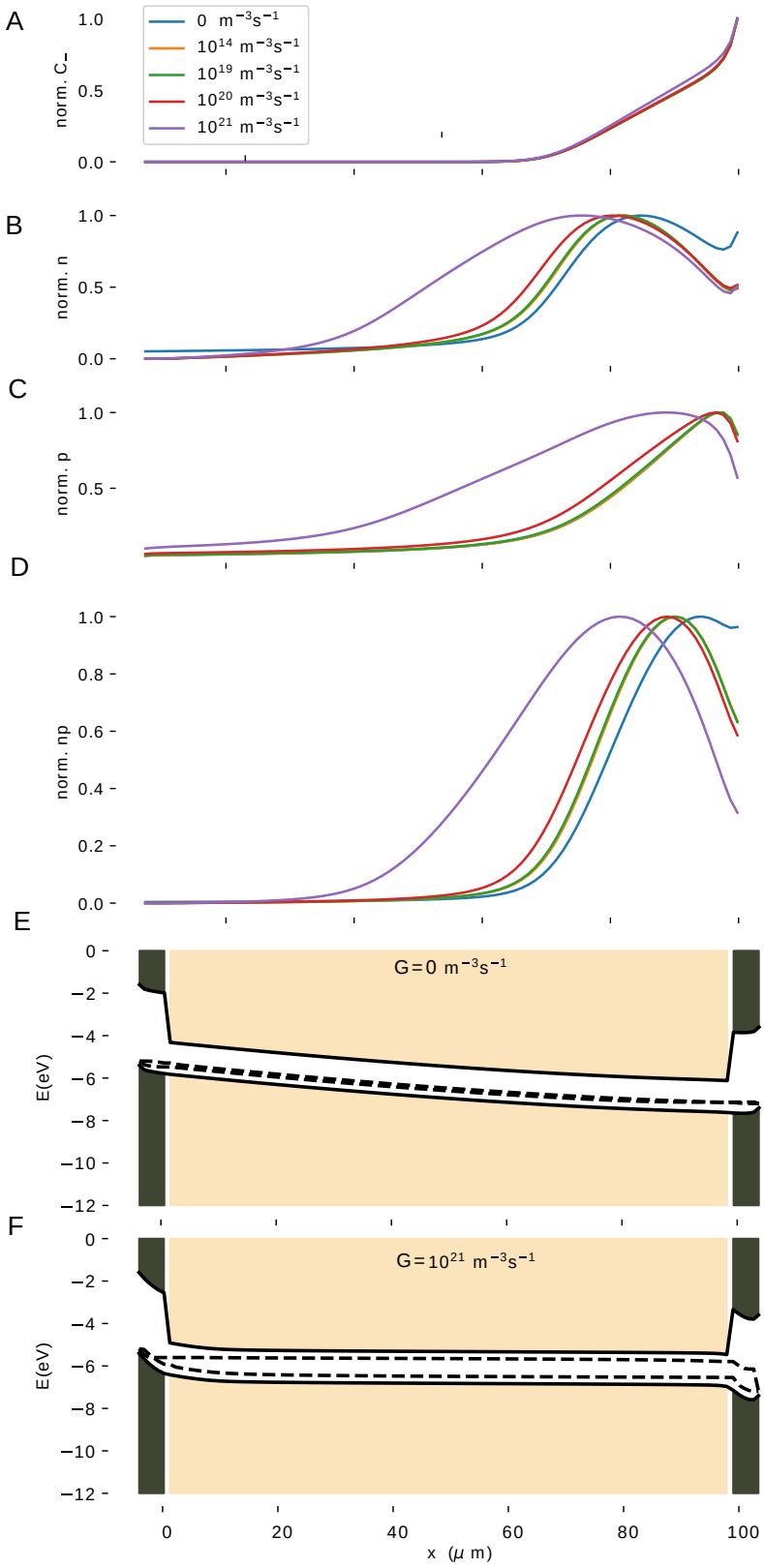

Figure 6.4: Illumination dependent simulations. Normalized concentrations of mobile anions **(A)**, electrons n **(B)**, holes p **(C)** and photoluminescence np **(D)** for different generation rates. Band diagrams and quasi-fermi levels for $G = 0$ **(E)**, $G = 10^{21} m^{-3} s^{-1}$ **(F)**.

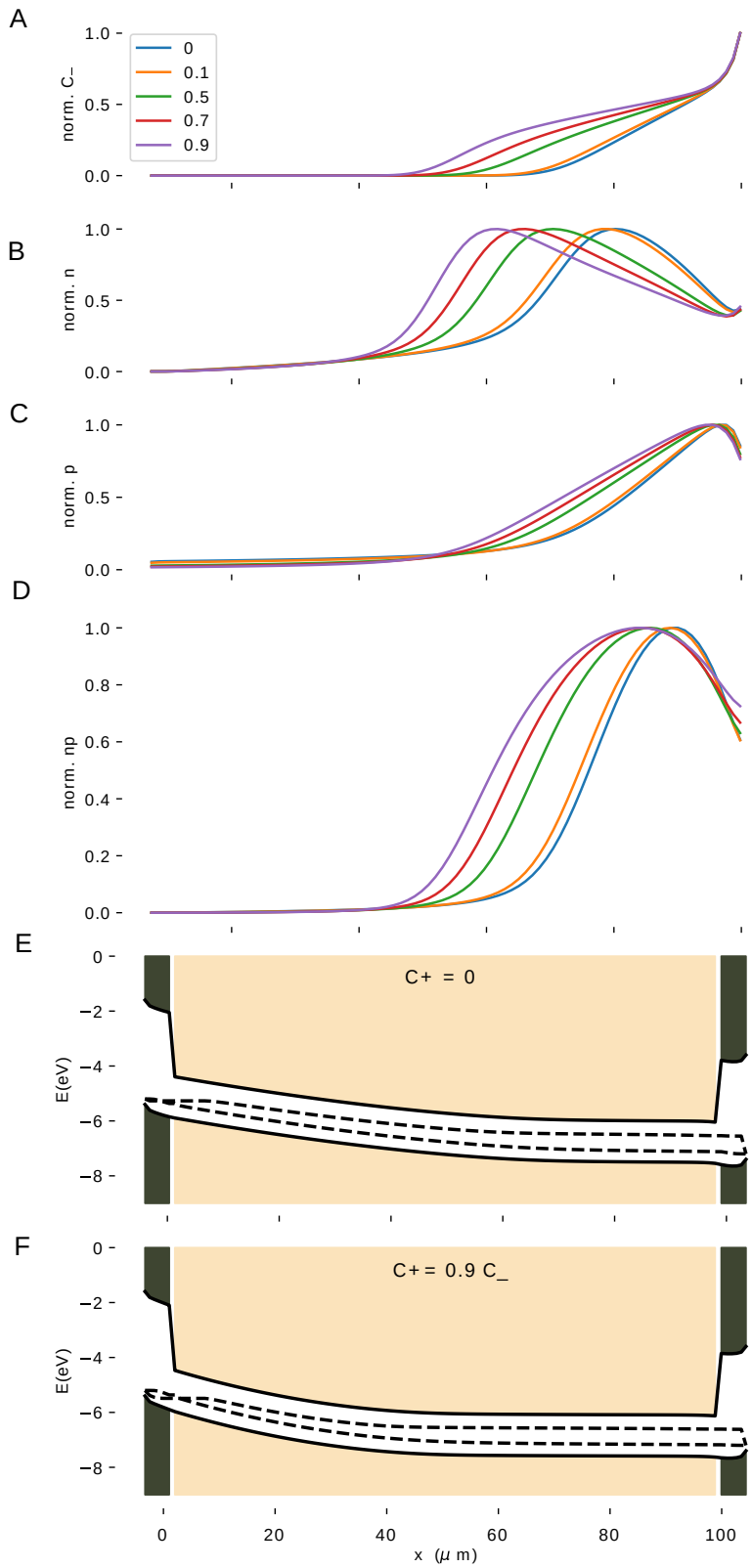

Figure 6.5: Simulations on p-doping. Normalized concentrations of mobile anions **(A)**, electrons n **(B)**, holes p **(C)** and photoluminescence np **(D)** for different ratios of immobile cations (C_+) to mobile ions (C_-). Band diagrams and quasi-fermi levels for $C_+ = 0$ **(E)** $C_+ = 0.9C_-$ **(F)**.

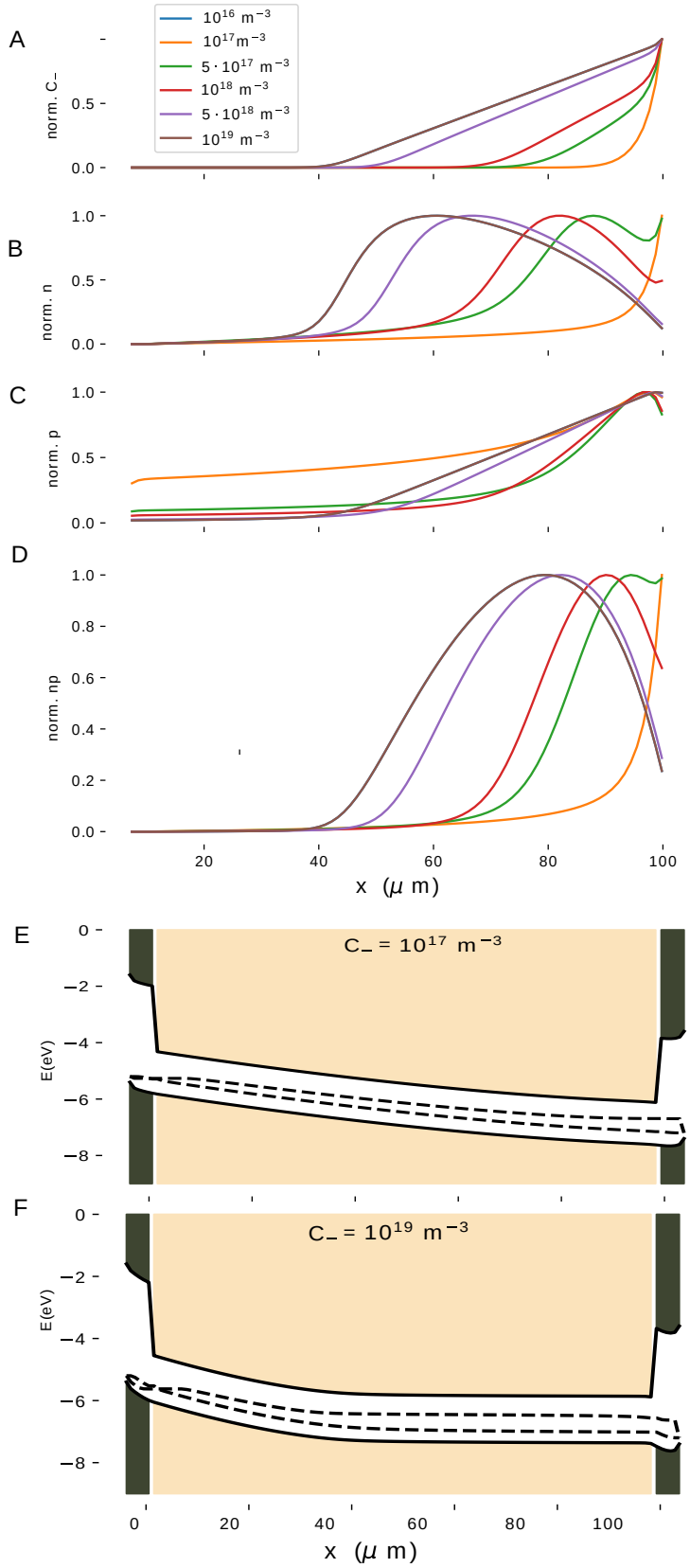

Figure 6.6: Ions dependent simulations under bias. Normalized concentrations of mobile anions **(A)**, electrons n **(B)**, holes p **(C)** and photoluminescence np **(D)** for different concentrations of mobile anions (C_-). Band diagrams and quasi-Fermi levels for $C_- = 10^{17}\mathrm{m}^{-3}$ **(E)** and $C = 10^{19}\mathrm{m}^{-3}$ **(F)**. This graph is the complete simulation of fig 7.4.

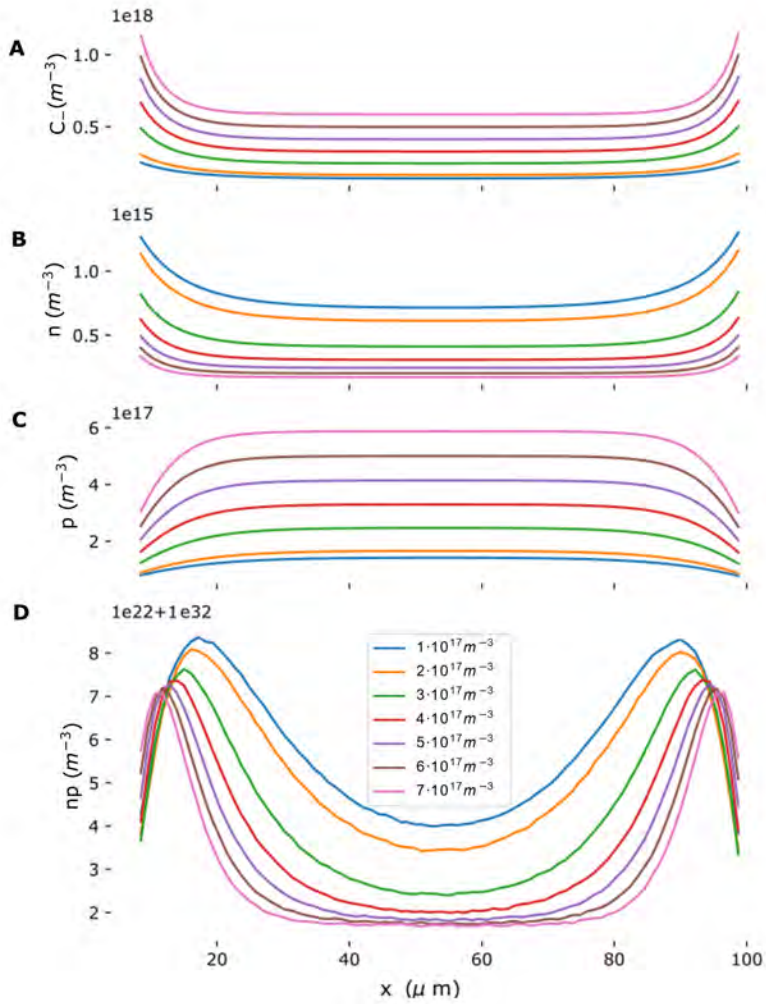

Figure 6.7: Ions dependent simulations at 0V. Concentrations of mobile anions **(A)**, electrons n **(B)**, holes p **(C)** and np **(D)** for different concentrations of mobile anions (C_-). This graph is the complete simulation of fig 7.2.

Discussion 7

7.1 Steady state PL at open circuit

The photoluminescence profile along the 100 μm device at 0V is displayed in fig. 7.1. It has a symmetrical shape, as expected, even though it is not uniform: peaked close to the transport layer interface and lower in the middle of the cell. This behaviour doesn't depend on the position of the device where the scan is performed, hence it is not due to the local variability in the chemical composition. In different batches, the distance of the peaks from the contact varies in the range $10-18\mu m$ while the ratio of minimum to maximum varies in the range $40-80\%$ (see Appendix A.2).

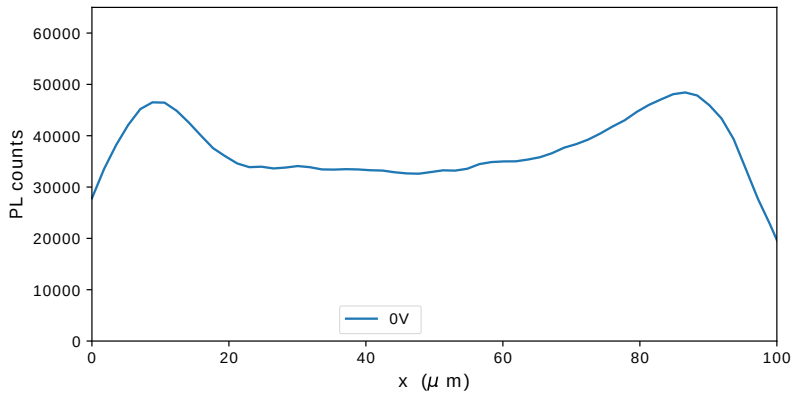

Figure 7.1: Measured steady state PL at 0V.

The reason of this inhomogeneity is yet to be understood since the simulated np concentration at 0V (fig. 7.2) is uniform. The trend observed in the experiments emerges when zooming in by several orders of magnitude since the signal to background ratio in the graph is 10^{-10}. The simulations suggest the accumulated ions at the interface, attracted by the built-in electric field, create a region of intense field at the interface, attracting carriers and generating the observed peaks in the PL.

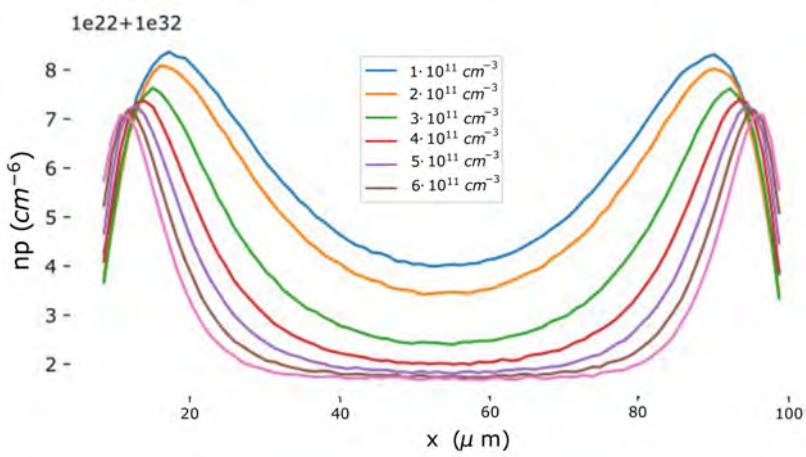

Figure 7.2: Simulated np at 0V for different mobile anion concentrations.

7.2 Steady state PL under bias

At 10 V, the PL distribution is asymmetrical as shown in fig. 7.3. It peaks in the middle of the device, towards the anode (right) and it is quenched but not completely at the interface with the cathode (left). The PL increases in the middle by 50 % and decreases at the cathode by 80 %.

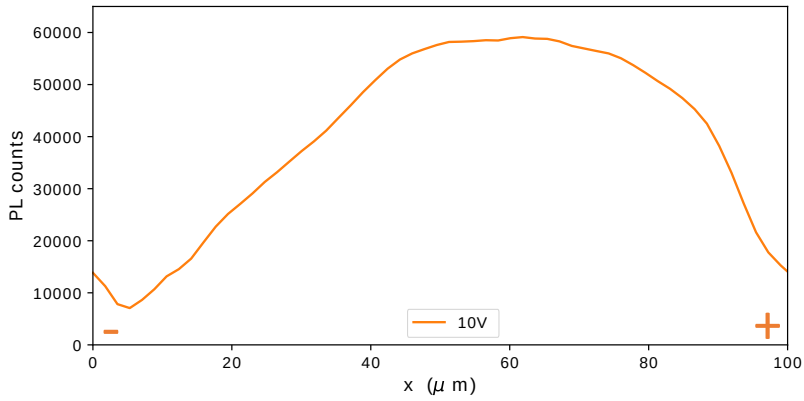

Figure 7.3: Measured steady state PL at 10V.

In this case, the simulated PL at 10 V qualitatively matches the measured PL, pointing at how the electrostatic repulsion of the ion accumulation layer might be the main process determining the distribution of charges and thus the PL along the device. Looking at fig. 7.4, for low ion concentrations (orange), electrons are concentrated on the anode and the PL peaks at the interface and decreases exponentially from the interface to the center. At higher anion concentrations, the negative ions accumulated at the interface repel the electrons, confining them in the center of the device and limiting their transport to the anode. This field screening at the interface could be the factor determining the increase in charge density in the middle of the device and thus the shift in the PL maximum from the anode towards the center.

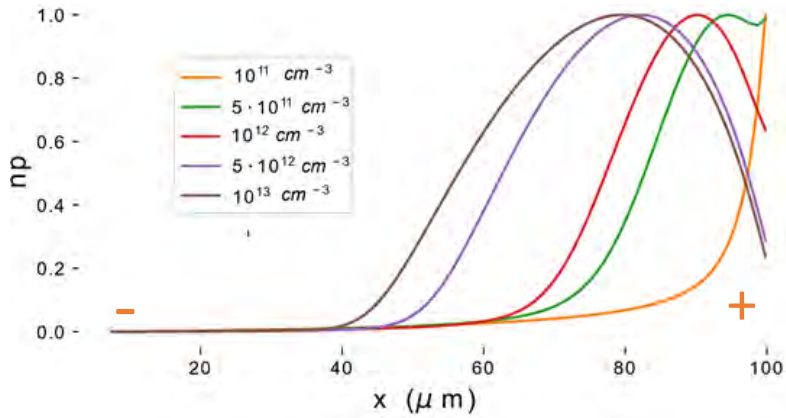

Figure 7.4: Simulated np at 10V for different mobile anion concentrations.

Further insights on the mechanism proposed here come from analyzing the band diagrams shown in fig. 7.5. With relatively low ion concentrations (top diagram), the band energies decrease linearly across the device, from cathode to anode. Hence, the electric field, which is the gradient of the potential, is constant across the device. With higher anion concentrations (bottom diagram), the accumulation layer at the anode is sufficient to screen the electric field, forming a flat band region in the middle-right of the device. This field-free region can span from the anode to the middle of the device, extending up to $70\mu m$. The drift of electrons towards the anode is limited, increasing the concentrations of electrons, as well as radiative recombination and PL, in the field-free region. At the cathode interface, the electric field is increased, since the energy-potential gradient is steeper, increasing the drift velocity of holes. Holes are transported and extracted more efficiently, thus decreasing the concentration of holes, as well as radiative recombination and PL, in the vicinity of the anode interface.

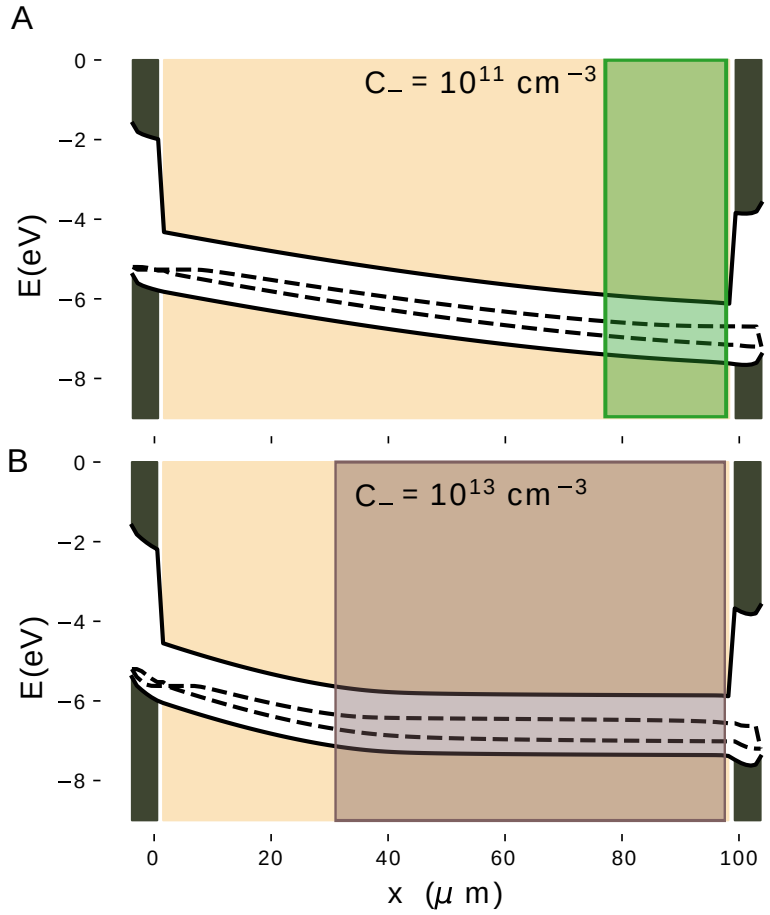

Figure 7.5: Simulated band diagram under bias at different ion concentrations. The band diagram at 2V (anode is on the right) of the device is displayed for different concentrations of mobile anions: **A)** low ion density $10^{11}\mathrm{cm}^{-3}$ and **B)** high ion density $10^{13}\mathrm{cm}^{-3}$. In the highlighted regions the PL is not quenched.

7.3 PL dynamics under bias

The steady-state PL profiles described in the section before do not interchange immediately when switching a bias. The transition between the steady states can be observed by measuring a succession one after the other, as described in section 5. It takes 0.06 s to measure the Pl spectrum at one point and move to the next and thus a 100 points line lasts 6s. For every fixed position, a point in the second line reports the PL measured 6 seconds after the PL in the first line. A point in the third line has a delay of 12 s and so forth. The transitions from the biased to the unbiased PL steady-state and vice-versa are shown in figure 7.6.

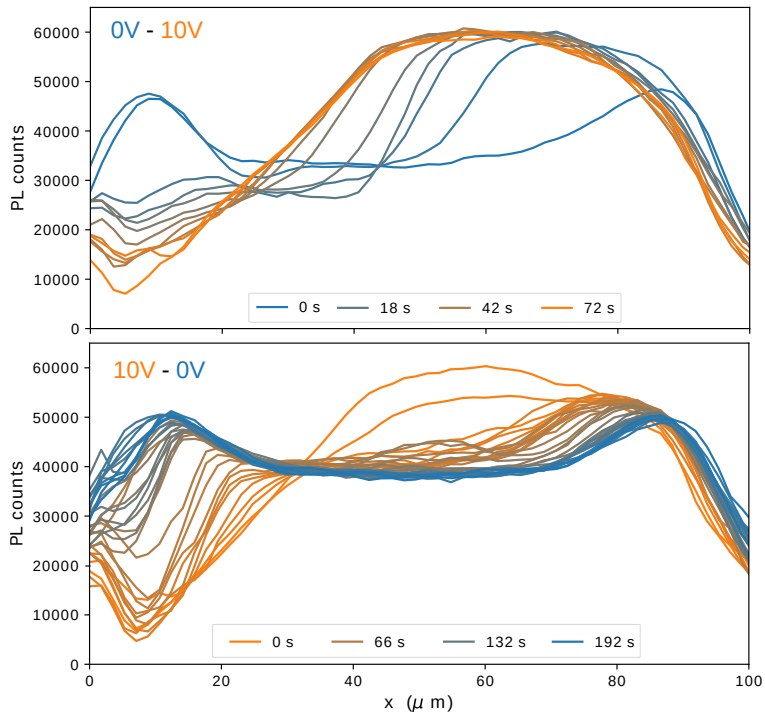

Figure 7.6: Time dependency of PL profile. In the top, drift-dominated transition between the 0V PL profile (blue) and the 10V PL profile (orange). The voltage and the time, start after the first scan is completed and each line scan lasts 6 s. In the bottom, diffusion-dominated transition from 10V PL profile (orange) and the 0V PL profile (blue).

First let's focus on the top graph, capturing the transition from 0 to 10 V. The device is initially at 0V. After scanning the first line, the voltage is switched to 10V. In the second line scan, the PL peak is already shifted away from the anode (right) meaning that some anions have already accumulated at the anode interface. At the cathode (left) interface the peak slowly decreases. The transition to the 10 V steady state is completed after 40s.

In the bottom graph, the device is initially at 10V and after the first line scan the voltage is switched off. The transition is twice as slow, since 0V steady state is reached after roughly 80s.

Following this work interpretation, these features can be explained by assuming that anions slowly drift to the anode interface. The more anions accumulate, the wider the field free region, hence the charge-rich and bright region. In short, anions drifting to the anode lead to *photoluminescence* drift away from it. At the same time, the region close to the cathode slowly darkens. This could be explained by the migration of anions leaving a uniform positively charged region, iodide vacancies. In

this region the electric field slowly increases, as well as the drift velocity of electrons and holes. Hence the cathode interface is progressively more depleted of holes and darkens.

Hence, the PL transient to the biased steady state is governed by the drift of ions. As soon as the voltage is switched on, the mobile anions are evenly distributed and there is no diffusion. Additionally, the electric field E is constant across the device. The drift current of ions can be written as

$$J = eCv = eC\mu E \tag{7.1}$$

where e is the elementary charge, C the concentration and μ the mobility. The mobility can be derived from the previous equation as

$$\mu = \frac{v}{E} \tag{7.2}$$

Let's assume that the velocity of the PL front is comparable to the velocity of the ions. In the first 30s the PL peak has moved roughly 30 μm, leading to an approximate velocity of $10^{-4} cm/s$. When the $10V$ bias is switched on, the electric field along the $100\mu m$ device is $10^3 Vcm$. The estimate of the mobility is then $10^{-7} cm^2/Vs$. More precisely this is an upper estimate of the mobility, since, when the diffusion current in the opposite direction is taken into consideration equation A.4 becomes

$$J = eCv < eC\mu E \tag{7.3}$$

and thus

$$\mu < \frac{v}{E} = 10^{-7} cm^2/Vs \tag{7.4}$$

This is a reliable upper estimate of the mobility of ions, which varies in the literature between $10^{-8} cm^2/Vs$ [110] and $10^{-9} cm^2/Vs$ [111].

The inverse transition happens when the voltage is switched off as shown in the bottom graph of fig. 7.6. In this case the transition is diffusion dominated. The accumulated anions diffuse back to a uniform distribution when the voltage is switched back.

7.4 Summary and Outlook

The total PL along a mixed halide mixed cation hole only, back contact, perovskite device is symmetric but non uniform at open circuit, displaying two peaks at roughly at $15\mu m$ from the hole transport layers. Under exposure to an electric field, the PL profile becomes asymmetric: the cathode peak is quenched, while the anode peak is enhanced and moves to the center of the device. The transition between the unbiased-to-biased PL profile, driven by the drift of ions, has a time-scale of roughly 40 s. On the other hand, the diffusion-driven relaxation from the biased PL to the unbiased PL happens in double the time, 80s. (see fig. 7.6).

The ionic specie -or species- involved in the quenching and enhancement of the PL under bias, and the mechanism by which the ions influence the charge carriers are not yet understood.

Nevertheless, steady-state simulations of the device, with one mobile anion, an immobile cation and no traps, are able to reproduce some features of the measured photoluminescence.

After the bias is switched on, mobile anions (possibly I^-) drift to the anode interface and screen the field. In the field-free region in the middle of the device, the transport of electrons and holes is limited and their direct recombination increases, leading to a PL enhancement. At the cathode interface the constant concentration of immobile cations (V_I^+) increases the electric field, thus extracting more holes and quenching the PL. After the voltage is switched off, the ions diffuse back to a uniform distribution and the unbiased photoluminescence profile is restored.

It is then possible to interpret the qualitative feature of the PL under bias just with electrostatic field screening of mobile ions. Band misalignment, change in trap density, interface chemistry, trap passivation, are neglected in the simulations and might not be the main mechanisms determining the PL behaviour in this device. This is in accordance with a paper from Thiesbrummel et al. published in 2021 [111], where they proposed that:

"*The loss in charge extraction efficiency and the PL increase in the device is due to the accumulation of electronic charges in the active layer. It is shown that the movement of mobile ions toward the interface inhibits charge extraction due to band flattening. It was found that the ionic charge density exceeded the injected carrier density by 2 orders of magnitude.*"

Still many aspects deserve further investigation. First, it is not clear what determines the unbiased photoluminescence profile. Further work is required in making the simulations converge for realistic parameters.

Second, it would be insightful to quantitatively derive an estimate of the ionic mobility through time-dependent drift-diffusion simulations. In order to do that, the simulation parameters need to be aligned with the experimental values.

Third, it is key to assess with imaging techniques (XRF) which ionic species migrate.

Fourth, the role of traps should be further investigated by measuring the change in non-radiative recombination coefficient k_1 with time-resolved PL under bias.

Fifth, new devices could be fabricated to determine the role of the transport layer and of the electrodes on the measurements. A Ni-NiOx device was fabricated during this project to avoid the electrochemical reactions that have been recorded with the Ag contact. Unfortunately, these devices didn't lead to any valuable result and further optimization of the annealing procedure is necessary.

Finally and most importantly. Ion migration deforms the band diagram flattening the band in the middle of the device while creating intense electric fields at the interfaces. Hence the transport of carriers is limited in the center and improved close to the interfaces. It is crucial to understand what are the global effects of ion accumulation on the extraction efficiency, hence performance, of a full perovskite solar cell. Is the performance of perovskites affected by the increased non-radiative recombination or by the decreased transport efficiency? Carrying these measurements on HTL/perovskite/ETL devices with the same architecture could bring interesting insights.

Appendix A

A.1 Dependence on different integration choices

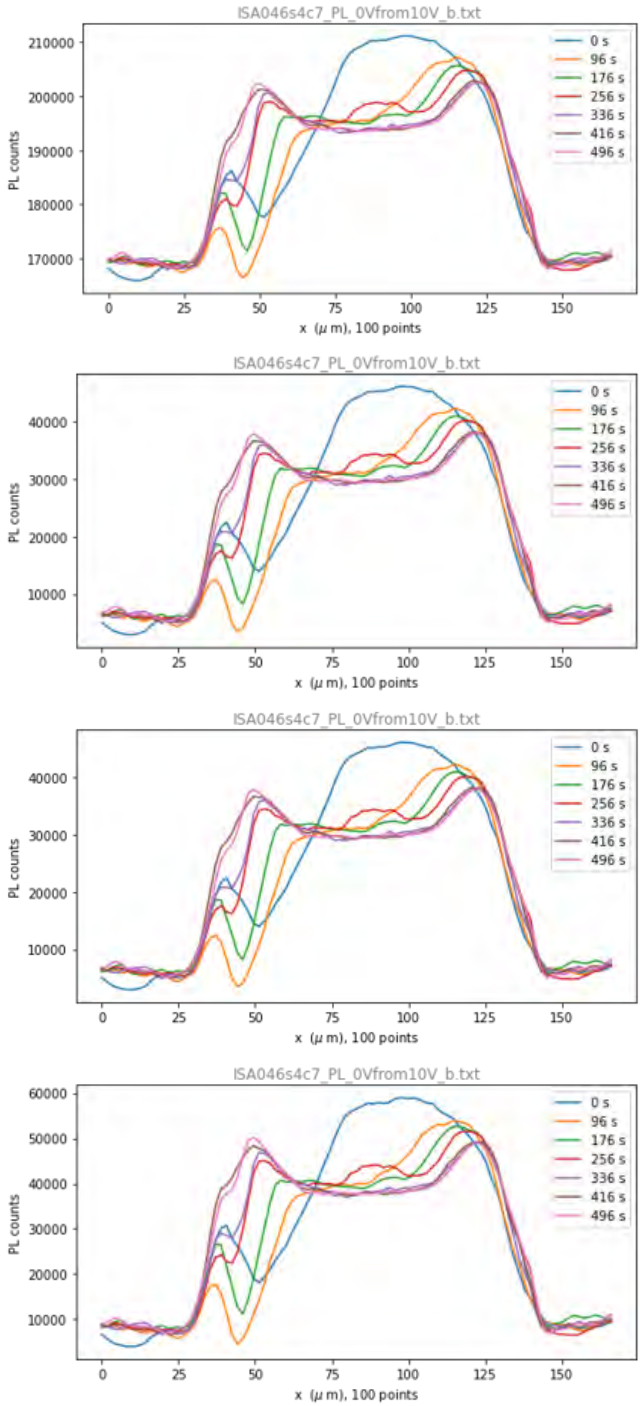

Figure A.1: The top two graphs confront the line scans for non-normalized PL signal (left) and normalized PL signal (right). The bottom ones compare the scans for different integration intervals $\Omega = \omega_0 \pm 20\mu m$ (left) and $\Omega = \omega_0 \pm 50\mu m$ (right).

A.2 Measurement reproducibility

One of the major hurdles of studying perovskite devices is the cell-to-cell, batch-to-batch and laboratory-to-laboratory reproducibility of the measurements. It could be due to the glovebox atmosphere or volume, to chemical impurities or stochiometric differences in the precursor mixture [112].

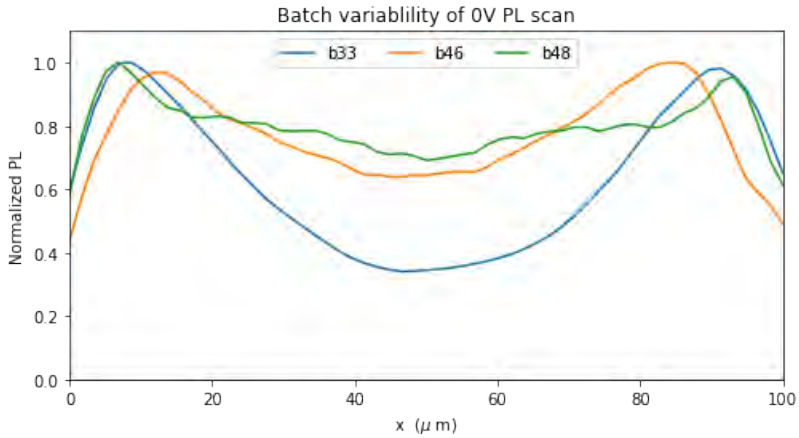

Figure A.2: Batch variability of the steady state PL scan at 0V.

The line scans vary slightly from batch to batch, though preserving the same trend. In b33 the PL quenching in the middle of the contact is much enhanced than in b46 and 48. This is most likely due to the different density of free ions, as shown in the simulations at different ion-concentrations 7.2. In b46 the peak positions are further from the contact. If one considers the PL spectra of the three batches in the middle of the perovskite, the central wavelength and standard deviation of the fitted gaussian do vary, as reported in the table.

Batch	ω_0	σ
b33	778 nm	18 nm
b46	772 nm	16 nm
b46	770 nm	16 nm

Table A.1: Cell variability of the PL spectral peak (ω_0) and width (ω_0) in the middle of the perovskite.

The variability between batches could be due to differences in the sythesis, as stechiometry of precursors, spin-coating conditions etc. The fact that the trend is reproductible is good news. The variability for different samples in on batch and different cells in the same sample is obviously much lower and probably due to the non homogeneous nature of the perovskite layer due to differences in local cristallization.

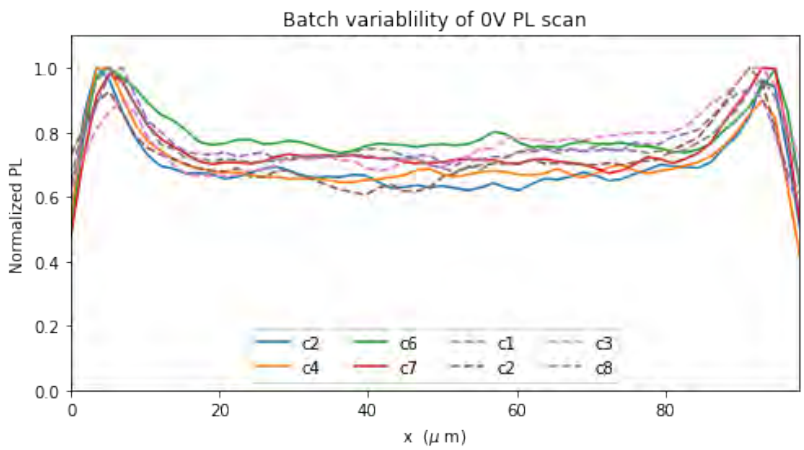

Figure A.3: Cell variability of the steady state PL scan at 0V for sample 5 (solid) and sample 6 (dashed) of batch 48.

A.3 PL time evolution at different positions

The graphs on PL time evolution in Figure 5.3 C are plotted at two fixed spatial positions along the device. The peak of the 0V PL ($15\mu m$) at the cathode and the peak of the 10 V PL ($62\mu m$) close to the anode were considered appropriate choices to track the dynamic of the peak. For the broad 10V peak (red), modifying the position by $3\mu m$ doesn't change the behaviour of the peak. For the narrower 0V left peak (green), a slight change in position alters the PL intensity, since it is much less uniform, but doesn't impact the timescale of the transition.

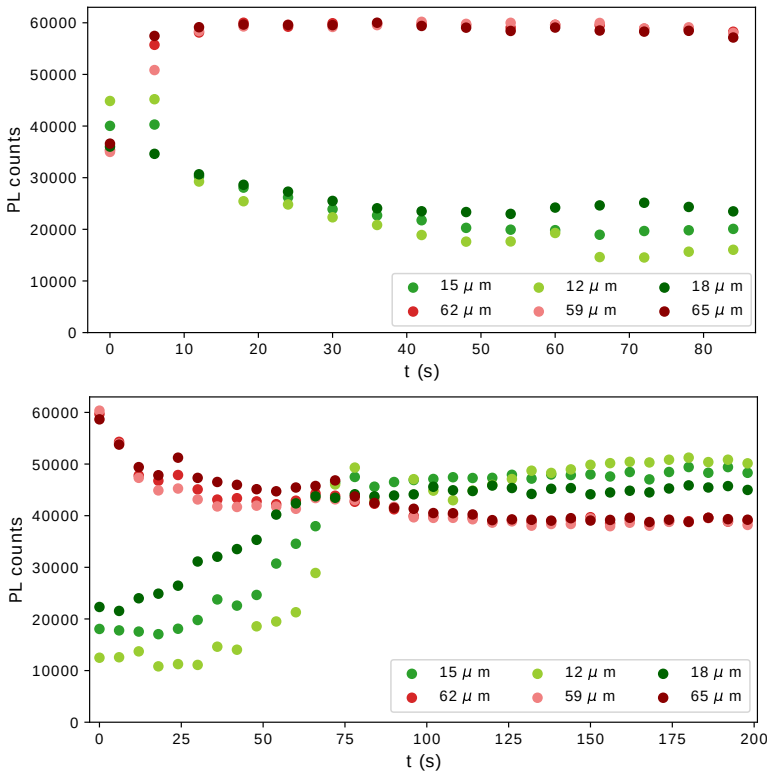

Figure A.4: Time dependent PL under bias at different positions: the top graphs shows the PL over time when a 10V bias is switched on, for different positions along the device. In the bottom graph, the voltage is switched off. The figure is equivalent to **??** C, but shows the behaviour of the left (red) and right (green) peak, for slightly changed positions.

The measurements give a photoluminescence signal dependent on three variables, wavelength λ, position along the device x and time t, $PL(x, t, \lambda)$. The photoluminescence spectrum is fitted to a gaussian, background subtracted and integrated over the full wavelength range, to obtain a space and time dependent photoluminescence $PL(x, t)$. This is plotted in figure **??** at few fixed positions or instants and as a colormap. Alternatively the peak wavelength can be plotted as a function of time and space $\lambda_0(x, t)$, to capture possible local changes in the crystalline structure and bangaps induced by the migration of ions, as reported in figure A.7.

A.4 Current measurements

The current measured during the transient PL measurement are reported in figure A.4. First of all, in the left graph it is evident how the current fluctuates. Indeed, during a line scan, when the laser is exciting electron-hole pairs in proximity of the cathode, the current is peaked since holes can be easily extracted. On the other hand, when the laser hovers above the anode, the photogenerated holes need to be transported all the way to the anode in order to generate current and electrons can't be extracted because of the energy barrier at the HTL interface. Hence the current is lower. Since the laser scans back and forth from cathode to anode the current oscillates.

In the right graph, the bias is switched off and the current still oscillates, but also decays exponentially to 0. We would expect this behaviour since at the 0V steady state the charges can't be extracted. The retarded decrease in current is an indication that ions accumulated at the interfaces create an internal field that transport charges, even when the external bias is off.

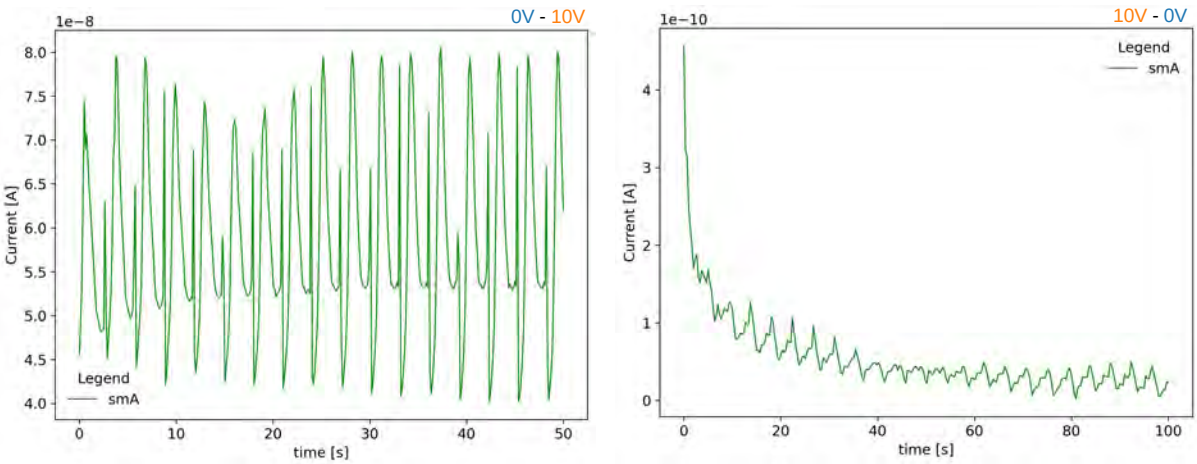

Figure A.5: Current measured during the PL measurements under bias. In the top graph, the current measurements starts after the 10V bias is applied. In the bottom graphs, the current measurement starts when the 10V bias is switched off.

A.5 PL red-shift

The PL in the region adjacent to the cathode not only is quenched but also red-shifted. As shown in fig. A.6, the peak wavelength in the cathode peak (15μm) shifts from roughly 773 nm at 0V to 771 nm at 2V. The peak

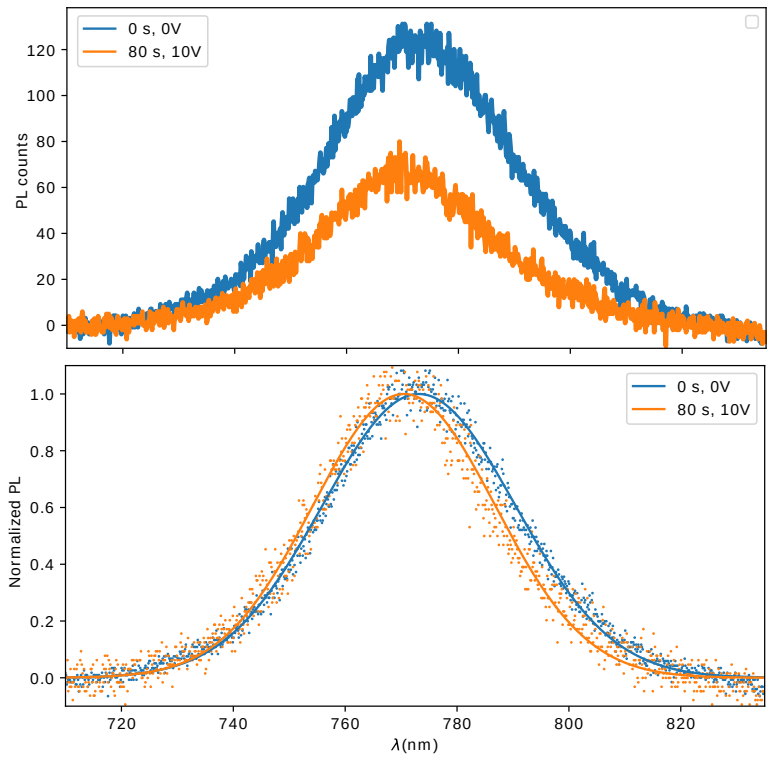

Figure A.6: PL quenching and peak shift at the anode. Comparison of the unbiased PL spectrum (blue) and PL spectrum at the 10V steady state (orange). The spectrum showed is 15μ away from the anode, where the 0V PL peaks and the 10V PL has a minimum. The background subtracted spectrum (top), can be fitted and normalized (bottom) to highlight the peak shift.

shift can also visualized with a t-x colormap of the peak wavelenght. For every time and position, the PL spectrum is fitted to a gaussian and the central position of the fitted curve is assumed to be the local bandgap wavelenght.

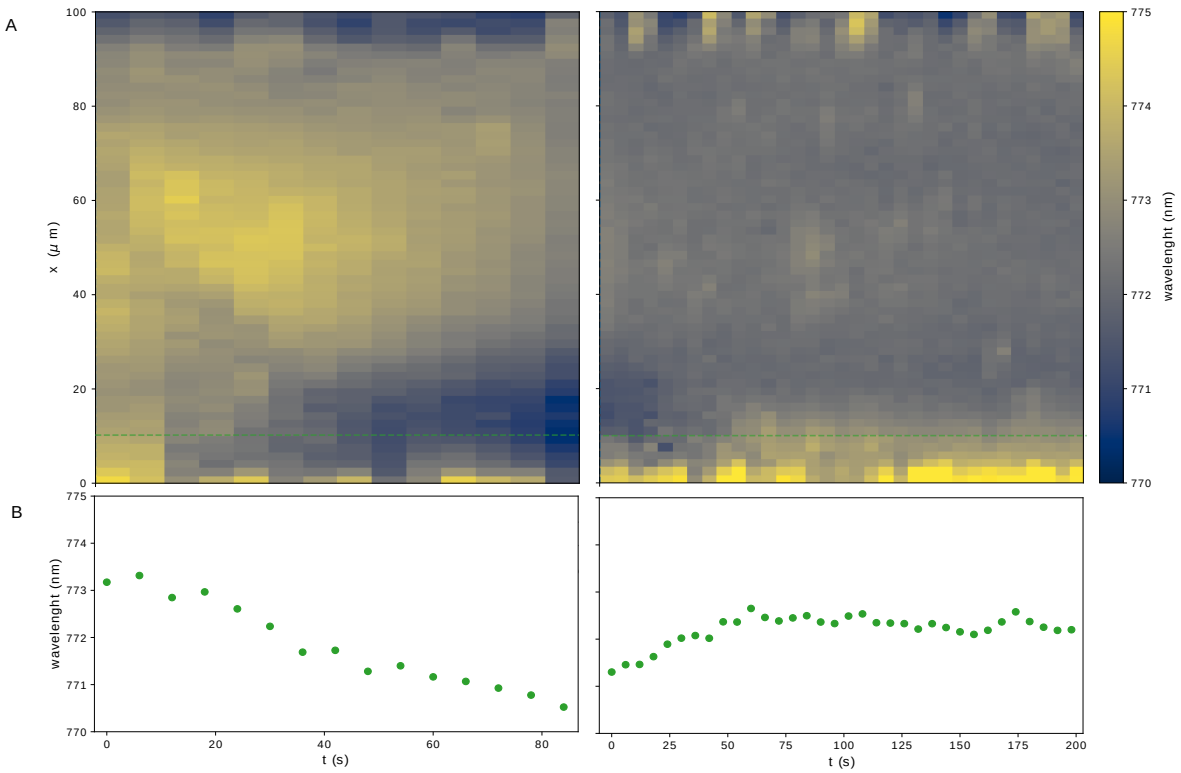

Figure A.7: PL peak shift under bias. **A)** Peak wavelength of the PL spectrum over time and space. The voltage is applied as in figure 5.3. **B)** Peak wavelenght over time above the 0 V maximum (x = 15μm).

Bibliography

Here are the references in citation order.

[1] J.G. Canadell et al. 'Global Carbon and other Biogeochemical Cycles and Feedbacks Supplementary Material'. In: *Climate Change 2021: The Physical Science Basis. Contribution of Working Group I to the Sixth Assessment Report of the Intergovernmental Panel on Climate Change*. Ed. by V. Masson-Delmotte et al. 2021 (cited on page 1).

[2] B. Bednar-Friedl et al. 'Europe'. In: *Climate Change 2022: Impacts, Adaptation and Vulnerability. Contribution of Working Group II to the Sixth Assessment Report of the Intergovernmental Panel on Climate Change*. Ed. by H. O. Pörtner et al. Cambridge, UK and New York, USA: Cambridge University Press, 2022, pp. 1817–1927. DOI: 10.1017/9781009325844.015.1817 (cited on page 1).

[3] B. Fox-Kemper et al. 'Ocean, Cryosphere and Sea Level Change'. In: *Climate Change 2021: The Physical Science Basis. Contribution of Working Group I to the Sixth Assessment Report of the Intergovernmental Panel on Climate Change*. Ed. by V. Masson-Delmotte et al. Cambridge, United Kingdom and New York, NY, USA: Cambridge University Press, 2021, pp. 1211–1362. DOI: 10.1017/9781009157896.011 (cited on page 1).

[4] H. Douville et al. 'Water Cycle Changes'. In: *Climate Change 2021: The Physical Science Basis. Contribution of Working Group I to the Sixth Assessment Report of the Intergovernmental Panel on Climate Change*. Ed. by V. Masson-Delmotte et al. Cambridge, United Kingdom and New York, NY, USA: Cambridge University Press, 2021, pp. 1055–1210. DOI: 10.1017/9781009157896.010 (cited on page 1).

[5] S.I. Seneviratne et al. 'Weather and Climate Extreme Events in a Changing Climate'. In: *Climate Change 2021: The Physical Science Basis. Contribution of Working Group I to the Sixth Assessment Report of the Intergovernmental Panel on Climate Change*. Ed. by V. Masson-Delmotte et al. Cambridge, United Kingdom and New York, NY, USA: Cambridge University Press, 2021, pp. 1513–1766. DOI: 10.1017/9781009157896.013 (cited on page 1).

[6] M.J. Costello et al. 'Cross-Chapter Paper 1: Biodiversity Hotspots'. In: *Climate Change 2022: Impacts, Adaptation and Vulnerability. Contribution of Working Group II to the Sixth Assessment Report of the Intergovernmental Panel on Climate Change*. Ed. by H. O. Pörtner et al. Cambridge, UK and New York, USA: Cambridge University Press, 2022, pp. 2123–2161. DOI: 10.1017/9781009325844.018.2123 (cited on page 1).

[7] Our world in data. *Global emissions by sector*. 2022. URL: https://ourworldindata.org/emissions-by-sector (cited on page 1).

[8] Monica Crippa et al. 'High resolution temporal profiles in the Emissions Database for Global Atmospheric Research'. In: *Scientific data* 7.1 (2020), pp. 1–17 (cited on page 1).

[9] IEA. 'Key World Energy Statistics 2021'. In: *IEA* (2021) (cited on page 1).

[10] IRENA. 'Renwable capacity highlights'. In: (2022) (cited on page 1).

[11] Yuan Tian and Chang-Ying Zhao. 'A review of solar collectors and thermal energy storage in solar thermal applications'. In: *Applied energy* 104 (2013), pp. 538–553 (cited on page 2).

[12] Michael Grätzel. 'Photoelectrochemical cells'. In: *nature* 414.6861 (2001), pp. 338–344 (cited on page 2).

[13] Lawrence L Kazmerski. 'Photovoltaics: A review of cell and module technologies'. In: *Renewable and sustainable energy reviews* 1.1-2 (1997), pp. 71–170 (cited on page 2).

[14] IEA. 'Electrification, IEA'. In: (2022) (cited on page 2).

[15] IRENA. *Renewable energy generation costs 2021*. 2021 (cited on page 2).

[16] Sunrun. 'how long do solar panels last?' In: () (cited on page 2).

[17] Zhengjie Zhu, Kaitian Mao, and Jixian Xu. 'Perovskite tandem solar cells with improved efficiency and stability'. In: *Journal of Energy Chemistry* 58 (2021), pp. 219–232 (cited on pages 2, 4).

[18] Louise C Hirst and Nicholas J Ekins-Daukes. 'Fundamental losses in solar cells'. In: *Progress in Photovoltaics: Research and Applications* 19.3 (2011), pp. 286–293 (cited on page 2).

[19] Clean Energy Reviews. *Most Efficient solar panels*. 2023. URL: https://www.cleanenergyreviews.info/blog/most-efficient-solar-panels (cited on page 2).

[20] NREL. *Best Research-cell Efficiency Chart*. 2022. URL: https://www.nrel.gov/pv/cell-efficiency.html (cited on pages 2, 3).

[21] Alexis De Vos. 'Detailed balance limit of the efficiency of tandem solar cells'. In: *Journal of Physics D: Applied Physics* 13.5 (1980), p. 839 (cited on page 2).

[22] Muhammad Tawalbeh et al. 'Environmental impacts of solar photovoltaic systems: A critical review of recent progress and future outlook'. In: *Science of The Total Environment* 759 (2021), p. 143528. DOI: https://doi.org/10.1016/j.scitotenv.2020.143528 (cited on page 2).

[23] Akihiro Kojima et al. 'Organometal halide perovskites as visible-light sensitizers for photovoltaic cells'. In: *Journal of the american chemical society* 131.17 (2009), pp. 6050–6051 (cited on page 3).

[24] T Jesper Jacobsson et al. 'An open-access database and analysis tool for perovskite solar cells based on the FAIR data principles'. In: *Nature Energy* 7.1 (2022), pp. 107–115 (cited on page 3).

[25] Jason J Yoo et al. 'Efficient perovskite solar cells via improved carrier management'. In: *Nature* 590.7847 (2021), pp. 587–593 (cited on page 3).

[26] Amran Al-Ashouri et al. 'Monolithic perovskite/silicon tandem solar cell with> 29% efficiency by enhanced hole extraction'. In: *Science* 370.6522 (2020), pp. 1300–1309 (cited on page 3).

[27] Wenjie Li et al. 'High-performance solar flow battery powered by a perovskite/silicon tandem solar cell'. In: *Nature materials* 19.12 (2020), pp. 1326–1331 (cited on page 3).

[28] Shuangyong Sun et al. 'The origin of high efficiency in low-temperature solution-processable bilayer organometal halide hybrid solar cells'. In: *Energy & Environmental Science* 7.1 (2014), pp. 399–407 (cited on page 3).

[29] Yuhei Ogomi et al. 'CH3NH3Sn x Pb (1–x) I3 Perovskite solar cells covering up to 1060 nm'. In: *The journal of physical chemistry letters* 5.6 (2014), pp. 1004–1011 (cited on page 3).

[30] Qingfeng Dong et al. 'Electron-hole diffusion lengths> 175 μm in solution-grown CH3NH3PbI3 single crystals'. In: *Science* 347.6225 (2015), pp. 967–970 (cited on page 3).

[31] Jun Kang and Lin-Wang Wang. 'High defect tolerance in lead halide perovskite CsPbBr3'. In: *The journal of physical chemistry letters* 8.2 (2017), pp. 489–493 (cited on page 3).

[32] Jinli Yang et al. 'Investigation of CH3NH3PbI3 degradation rates and mechanisms in controlled humidity environments using in situ techniques'. In: *ACS nano* 9.2 (2015), pp. 1955–1963 (cited on page 3).

[33] Nicholas Aristidou et al. 'The role of oxygen in the degradation of methylammonium lead trihalide perovskite photoactive layers'. In: *Angewandte Chemie* 127.28 (2015), pp. 8326–8330 (cited on page 3).

[34] Zhiping Wang et al. 'Efficient ambient-air-stable solar cells with 2D–3D heterostructured butylammonium-caesium-formamidinium lead halide perovskites'. In: *Nature Energy* 2.9 (2017), pp. 1–10 (cited on page 3).

[35] Giorgio Divitini et al. 'In situ observation of heat-induced degradation of perovskite solar cells'. In: *Nature Energy* 1.2 (2016), pp. 1–6 (cited on page 3).

[36] Jing Wei et al. 'Mechanisms and suppression of photoinduced degradation in perovskite solar cells'. In: *Advanced Energy Materials* 11.3 (2021), p. 2002326 (cited on page 3).

[37] Peng Zhou et al. 'Efficient and stable mixed perovskite solar cells using P3HT as a hole transporting layer'. In: *Journal of Materials Chemistry C* 6.21 (2018), pp. 5733–5737 (cited on page 3).

[38] Hsin-Hsiang Huang et al. 'Boosting the ultra-stable unencapsulated perovskite solar cells by using montmorillonite/CH 3 NH 3 PbI 3 nanocomposite as photoactive layer'. In: *Energy & Environmental Science* 12.4 (2019), pp. 1265–1273 (cited on page 3).

[39] Yousheng Wang et al. 'Fully-ambient-air and antisolvent-free-processed stable perovskite solar cells with perovskite-based composites and interface engineering'. In: *Nano Energy* 64 (2019), p. 103964 (cited on page 3).

[40] Laura Calio et al. 'A generic route of hydrophobic doping in hole transporting material to increase longevity of perovskite solar cells'. In: *Joule* 2.9 (2018), pp. 1800–1815 (cited on page 3).

[41] Chih-Yu Chang, Wen-Kuan Huang, and Yu-Chia Chang. 'Highly-efficient and long-term stable perovskite solar cells enabled by a cross-linkable n-doped hybrid cathode interfacial layer'. In: *Chemistry of Materials* 28.17 (2016), pp. 6305–6312 (cited on page 3).

[42] Chan-Hee Jung et al. 'Polyacrylonitrile-grafted reduced graphene oxide hybrid: An all-round and efficient hole-extraction material for organic and inorganic-organic hybrid photovoltaics'. In: *Nano Energy* 31 (2017), pp. 19–27 (cited on page 3).

[43] Mark V Khenkin et al. 'Consensus statement for stability assessment and reporting for perovskite photovoltaics based on ISOS procedures'. In: *Nature Energy* 5.1 (2020), pp. 35–49 (cited on page 3).

[44] Weijun Ke and Mercouri G Kanatzidis. 'Prospects for low-toxicity lead-free perovskite solar cells'. In: *Nature communications* 10.1 (2019), p. 965 (cited on page 3).

[45] Nam-Gyu Park. 'Green solvent for perovskite solar cell production'. In: *Nature Sustainability* 4.3 (2021), pp. 192–193 (cited on page 3).

[46] Jin Young Kim et al. 'High-efficiency perovskite solar cells'. In: *Chemical Reviews* 120.15 (2020), pp. 7867–7918 (cited on page 4).

[47] Katelyn P Goetz et al. 'Shining light on the photoluminescence properties of metal halide perovskites'. In: *Advanced Functional Materials* 30.23 (2020), p. 1910004 (cited on page 4).

[48] Hongwei Zhu et al. 'Efficient and stable large bandgap MAPbBr3 perovskite solar cell attaining an open circuit voltage of 1.65 V'. In: *ACS Energy Letters* 7.3 (2022), pp. 1112–1119 (cited on page 4).

[49] Tim Hellmann et al. 'The electronic structure of MAPI-based perovskite solar cells: Detailed band diagram determination by photoemission spectroscopy comparing classical and inverted device stacks'. In: *Advanced Energy Materials* 10.42 (2020), p. 2002129 (cited on page 4).

[50] Simone Meloni et al. 'Valence and conduction band tuning in halide perovskites for solar cell applications'. In: *Journal of Materials Chemistry A* 4.41 (2016), pp. 15997–16002 (cited on page 4).

[51] Norman Pellet et al. 'Mixed-organic-cation Perovskite photovoltaics for enhanced solar-light harvesting'. In: *Angewandte chemie* 126.12 (2014), pp. 3215–3221 (cited on page 4).

[52] Emanuele Smecca et al. 'Stability of solution-processed MAPbI 3 and FAPbI 3 layers'. In: *Physical Chemistry Chemical Physics* 18.19 (2016), pp. 13413–13422 (cited on page 4).

[53] David P McMeekin et al. 'A mixed-cation lead mixed-halide perovskite absorber for tandem solar cells'. In: *Science* 351.6269 (2016), pp. 151–155 (cited on pages 4, 10, 11, 25).

[54] Jun Hong Noh et al. 'Chemical management for colorful, efficient, and stable inorganic–organic hybrid nanostructured solar cells'. In: *Nano letters* 13.4 (2013), pp. 1764–1769 (cited on page 4).

[55] Dongxu Lin et al. 'Ion migration accelerated reaction between oxygen and metal halide perovskites in light and its suppression by cesium incorporation'. In: *Advanced Energy Materials* 11.8 (2021), p. 2002552 (cited on page 4).

[56] Zhuang Zhang et al. 'Big data driven perovskite solar cell stability analysis'. In: *Nature Communications* 13.1 (2022), pp. 1–10 (cited on page 4).

[57] Xin Yan et al. 'Ion migration in hybrid perovskites: Classification, identification, and manipulation'. In: *Nano Today* 44 (2022), p. 101503 (cited on pages 5, 26).

[58] Guang Yang et al. 'Interface engineering in planar perovskite solar cells: energy level alignment, perovskite morphology control and high performance achievement'. In: *Journal of Materials Chemistry A* 5.4 (2017), pp. 1658–1666 (cited on page 5).

[59] Christopher Eames et al. 'Ionic transport in hybrid lead iodide perovskite solar cells'. In: *Nature communications* 6.1 (2015), p. 7497 (cited on page 5).

[60] Yuichi Kato et al. 'Silver iodide formation in methyl ammonium lead iodide perovskite solar cells with silver top electrodes'. In: *Advanced Materials Interfaces* 2.13 (2015), p. 1500195 (cited on pages 5, 26).

[61] Olga R Yamilova et al. 'Reduction of methylammonium cations as a major electrochemical degradation pathway in MAPbI3 perovskite solar cells'. In: *The Journal of Physical Chemistry Letters* 11.1 (2019), pp. 221–228 (cited on pages 5, 26).

[62] Monojit Bag et al. 'Kinetics of ion transport in perovskite active layers and its implications for active layer stability'. In: *Journal of the American Chemical Society* 137.40 (2015), pp. 13130–13137 (cited on page 5).

[63] Philip Calado et al. 'Evidence for ion migration in hybrid perovskite solar cells with minimal hysteresis'. In: *Nature communications* 7.1 (2016), p. 13831 (cited on pages 5, 7).

[64] Wan-Jian Yin, Tingting Shi, and Yanfa Yan. 'Unusual defect physics in CH3NH3PbI3 perovskite solar cell absorber'. In: *Applied Physics Letters* 104.6 (2014), p. 063903 (cited on page 5).

[65] Tomas Leijtens et al. 'Mapping electric field-induced switchable poling and structural degradation in hybrid lead halide perovskite thin films'. In: *Advanced Energy Materials* 5.20 (2015), p. 1500962 (cited on page 5).

[66] Jing Zhang et al. 'Extrinsic movable ions in MAPbI3 modulate energy band alignment in perovskite solar cells'. In: *Advanced Energy Materials* 8.5 (2018), p. 1701981 (cited on page 5).

[67] Elizabeth M Tennyson et al. 'Cesium-incorporated triple cation perovskites deliver fully reversible and stable nanoscale voltage response'. In: *ACS nano* 13.2 (2018), pp. 1538–1546 (cited on page 5).

[68] Emily C Smith et al. 'Interplay between ion transport, applied bias, and degradation under illumination in hybrid perovskite pin devices'. In: *The Journal of Physical Chemistry C* 122.25 (2018), pp. 13986–13994 (cited on page 5).

[69] Dong Wei et al. 'Ion-migration inhibition by the cation–π interaction in perovskite materials for efficient and stable perovskite solar cells'. In: *Advanced Materials* 30.31 (2018), p. 1707583 (cited on page 5).

[70] Yongbo Yuan et al. 'Photovoltaic switching mechanism in lateral structure hybrid perovskite solar cells'. In: *Advanced Energy Materials* 5.15 (2015), p. 1500615 (cited on page 5).

[71] Eric T Hoke et al. 'Reversible photo-induced trap formation in mixed-halide hybrid perovskites for photovoltaics'. In: *Chemical Science* 6.1 (2015), pp. 613–617 (cited on page 5).

[72] Dane W DeQuilettes et al. 'Photo-induced halide redistribution in organic–inorganic perovskite films'. In: *Nature communications* 7.1 (2016), p. 11683 (cited on page 5).

[73] Yupeng Zhang et al. 'Reversible structural swell–shrink and recoverable optical properties in hybrid inorganic–organic perovskite'. In: *Acs Nano* 10.7 (2016), pp. 7031–7038 (cited on page 5).

[74] Martin Stolterfoht et al. 'Voltage-dependent photoluminescence and how it correlates with the fill factor and open-circuit voltage in perovskite solar cells'. In: *ACS Energy Letters* 4.12 (2019), pp. 2887–2892 (cited on page 6).

[75] Tomas Leijtens et al. 'Modulating the electron–hole interaction in a hybrid lead halide perovskite with an electric field'. In: *Journal of the American Chemical Society* 137.49 (2015), pp. 15451–15459 (cited on page 6).

[76] Samuel D Stranks et al. 'Recombination kinetics in organic-inorganic perovskites: excitons, free charge, and subgap states'. In: *Physical Review Applied* 2.3 (2014), p. 034007 (cited on page 6).

[77] Xiaofan Deng et al. 'Electric field induced reversible and irreversible photoluminescence responses in methylammonium lead iodide perovskite'. In: *Journal of Materials Chemistry C* 4.38 (2016), pp. 9060–9068 (cited on page 6).

[78] Daniel L Jacobs et al. 'Voltage-induced transients in methylammonium lead triiodide probed by dynamic photoluminescence spectroscopy'. In: *The Journal of Physical Chemistry C* 120.15 (2016), pp. 7893–7902 (cited on page 6).

[79] Alessandro Senocrate et al. 'The nature of ion conduction in methylammonium lead iodide: a multimethod approach'. In: *Angewandte Chemie* 129.27 (2017), pp. 7863–7867 (cited on page 6).

[80] Cheng Li et al. 'Real-time observation of iodide ion migration in methylammonium lead halide Perovskites'. In: *Small* 13.42 (2017), p. 1701711 (cited on page 6).

[81] Cheng Li et al. 'Unravelling the role of vacancies in lead halide perovskite through electrical switching of photoluminescence'. In: *Nature communications* 9.1 (2018), p. 5113 (cited on pages 6, 26).

[82] Susanne T Birkhold et al. 'Interplay of mobile ions and injected carriers creates recombination centers in metal halide perovskites under bias'. In: *ACS Energy Letters* 3.6 (2018), pp. 1279–1286 (cited on page 6).

[83] Ronen Gottesman et al. 'Dynamic phenomena at perovskite/electron-selective contact interface as interpreted from photovoltage decays'. In: *Chem* 1.5 (2016), pp. 776–789 (cited on page 7).

[84] Simon EJ O'Kane et al. 'Measurement and modelling of dark current decay transients in perovskite solar cells'. In: *Journal of Materials Chemistry C* 5.2 (2017), pp. 452–462 (cited on page 7).

[85] Stephan van Reenen, Martijn Kemerink, and Henry J Snaith. 'Modeling anomalous hysteresis in perovskite solar cells'. In: *The journal of physical chemistry letters* 6.19 (2015), pp. 3808–3814 (cited on page 7).

[86] Pilar Lopez-Varo et al. 'Device physics of hybrid perovskite solar cells: theory and experiment'. In: *Advanced Energy Materials* 8.14 (2018), p. 1702772 (cited on page 7).

[87] Marten Koopmans, Vincent M Le Corre, and L Jan Anton Koster. 'SIMsalabim: An open-source drift-diffusion simulator for semiconductor devices'. In: *Journal of Open Source Software* 7.70 (2022), p. 3727 (cited on page 7).

[88] L Jan Anton Koster et al. 'Quantifying bimolecular recombination losses in organic bulk heterojunction solar cells'. In: *Advanced Materials* 23.14 (2011), pp. 1670–1674 (cited on page 7).

[89] Vincent M Le Corre et al. 'Identification of the dominant recombination process for perovskite solar cells based on machine learning'. In: *Cell Reports Physical Science* 2.2 (2021), p. 100346 (cited on page 7).

[90] Davide Bartesaghi et al. 'Competition between recombination and extraction of free charges determines the fill factor of organic solar cells'. In: *Nature communications* 6.1 (2015), p. 7083 (cited on page 7).

[91] Vincent M Le Corre et al. 'Revealing charge carrier mobility and defect densities in metal halide perovskites via space-charge-limited current measurements'. In: *ACS energy letters* 6.3 (2021), pp. 1087–1094 (cited on pages 7, 25).

[92] Marten Koopmans and L Jan Anton Koster. 'Voltage Deficit in Wide Bandgap Perovskite Solar Cells: The Role of Traps, Band Energies, and Effective Density of States'. In: *Solar RRL* (2022), p. 2200560 (cited on page 7).

[93] Vincent M Le Corre et al. 'Charge transport layers limiting the efficiency of perovskite solar cells: how to optimize conductivity, doping, and thickness'. In: *ACS Applied Energy Materials* 2.9 (2019), pp. 6280–6287 (cited on page 7).

[94] Mejd Alsari et al. 'In situ simultaneous photovoltaic and structural evolution of perovskite solar cells during film formation'. In: *Energy & Environmental Science* 11.2 (2018), pp. 383–393 (cited on page 17).

[95] AN Jumabekov et al. 'Back-contacted hybrid organic–inorganic perovskite solar cells'. In: *Journal of Materials Chemistry C* 4.15 (2016), pp. 3125–3130 (cited on page 17).

[96] Chen-Fu Lin et al. 'Back-contact perovskite solar cells'. In: *Semiconductor Science and Technology* 36.8 (2021), p. 083001 (cited on page 17).

[97] Marten Koopmans, Vincent Corre, and L Koster. 'Simsalabim: An open-source drift-diffusion simulator for semiconductor devices'. In: *J. Open Source Softw.* 7.70 (Feb. 2022), p. 3727 (cited on page 24).

[98] Weihong Chang et al. 'Simulation of innovative high efficiency perovskite solar cell with Bi-HTL: NiO and Si thin films'. In: *Solar Energy* 186 (2019), pp. 323–327 (cited on page 25).

[99] Guochuan Fang et al. 'Optimized analysis of back-contact perovskite solar cells architectures'. In: *Optik* 207 (2020), p. 164362 (cited on page 25).

[100] Lisa Krückemeier et al. 'Understanding transient photoluminescence in halide perovskite layer stacks and solar cells'. In: *Advanced Energy Materials* 11.19 (2021), p. 2003489 (cited on page 25).

[101] Laura M Herz. 'Charge-carrier mobilities in metal halide perovskites: fundamental mechanisms and limits'. In: *ACS Energy Letters* 2.7 (2017), pp. 1539–1548 (cited on page 25).

[102] Elisabeth A Duijnstee et al. 'Understanding dark current-voltage characteristics in metal-halide perovskite single crystals'. In: *Physical Review Applied* 15.1 (2021), p. 014006 (cited on pages 25, 26).

[103] Michael D Irwin et al. 'p-Type semiconducting nickel oxide as an efficiency-enhancing anode interfacial layer in polymer bulk-heterojunction solar cells'. In: *Proceedings of the National Academy of Sciences* 105.8 (2008), pp. 2783–2787 (cited on page 25).

[104] KV Rao and A Smakula. 'Dielectric properties of cobalt oxide, nickel oxide, and their mixed crystals'. In: *Journal of Applied Physics* 36.6 (1965), pp. 2031–2038 (cited on page 25).

[105] Stephen Fonash. *Solar cell device physics*. Elsevier, 2012 (cited on page 25).

[106] SJ Handley and GW Bradberry. 'Estimates of charge carrier mobility and lifetime in nickel oxide'. In: *Physics Letters A* 40.4 (1972), pp. 277–278 (cited on page 25).

[107] Johannes M Richter et al. 'Enhancing photoluminescence yields in lead halide perovskites by photon recycling and light out-coupling'. In: *Nature communications* 7.1 (2016), pp. 1–8 (cited on page 26).

[108] Luca Bertoluzzi et al. 'Mobile ion concentration measurement and open-access band diagram simulation platform for halide perovskite solar cells'. In: *Joule* 4.1 (2020), pp. 109–127 (cited on page 26).

[109] Aron Walsh et al. 'Self-regulation mechanism for charged point defects in hybrid halide perovskites'. In: *Angewandte Chemie* 127.6 (2015), pp. 1811–1814 (cited on page 26).

[110] Vincent M Le Corre et al. 'Quantification of efficiency losses due to mobile ions in perovskite solar cells via fast hysteresis measurements'. In: *Solar RRL* 6.4 (2022), p. 2100772 (cited on page 37).

[111] Jarla Thiesbrummel et al. 'Universal current losses in perovskite solar cells due to mobile ions'. In: *Advanced Energy Materials* 11.34 (2021), p. 2101447 (cited on pages 37, 38).

[112] Paul Fassl et al. 'Fractional deviations in precursor stoichiometry dictate the properties, performance and stability of perovskite photovoltaic devices'. In: *Energy & environmental science* 11.12 (2018), pp. 3380–3391 (cited on page 42).

Notation

The next list describes several symbols that will be later used within the body of the document.

β	inverse of the thermal energy
ΔE_F	quasi-Fermi level splitting
ε	electric permittivity
μ	mobility
φ	flux
φ	photon flux
ρ	charge density
σ	trap cross section
C	ion concentration
c	speed of light in a vacuum inertial frame
c_n	electron trap capture rate
D	diffusion coefficient
d	penetration depth
E	electric field
e	elementary charge
E_C	conduction band energy
E_F	Fermi energy
E_G	bandgap energy
E_V	valence band energy
E_{fn}	electron quasi-Fermi level
E_{fp}	hole quasi-Fermi level
FF	fill factor
G	generation rate
G_{th}	thermal generation rate
h	Planck constant
I_{in}	Incident irradiance
J	current density

J_{SC}	short circut current density
k	Boltzmann constant
k_1	trap-assisted recombination constant
k_2	direct recombination constant
k_3	third order recombination constant
L	diffusion lenght
l	device length
m^*	effective mass
n	electron concentration under illumination
n_0	electron concentration in the dark
N_C	density of states of the conduction band
N_T	density of traps
N_V	density of states of the valence band
p	electron concentration under illumination
p_0	hole concentration at in the dark
R	recombination rate
R_1	trap-assisted recombination rate
R_2	direct recombination rate
R_3	Auger recombination rate
R_{bulk}	bulk trap-assisted recombination rate
R_{surf}	surface trap-assisted recombination rate
R_{th}	thermal recombination rate
S_r	surface recombination velocity
T	temperature
V	electric potential
v	velocity
V_b	bias voltage
V_{OC}	open circuit potential
v_{th}	thermal velocity